

REPORT DOCUMENTATION PAGE

0329

Public reporting burden for this collection of information is estimated to average 1 hour per response, including the time for reviewing instructions, searching existing data sources, gathering and maintaining the data needed and completing and reviewing the collection of information. Send comments regarding this burden estimate or any other aspect of the collection of information, including suggestions for reducing the burden to Washington Headquarters Services, Directorate for Information Operations and Reports, 1215 Jefferson Davis Highway, Suite 1204, Arlington, VA 22202-4302 and to the Office of Management and Budget, Paperwork Reduction Project (5704-0189), Washington, DC 20503

1. AGENCY USE ONLY (Leave blank)		2. REPORT DATE June 1997	3. REPORT TYPE AND DATES COVERED Final 01 Mar 95 - 28 Feb 97	
4. TITLE AND SUBTITLE OF REPORT Visible Upconversion Lasers -- Fiber and Planar Waveguide Devices			5. FUNDING NUMBERS 61102F 2301/AS	
6. AUTHOR(S) J. G. Eden			7. PERFORMING ORGANIZATION REPORT NUMBER:	
7. PERFORMING ORGANIZATION NAME(S) AND ADDRESS(ES) Board of Trustees of the University of Illinois 801 S. Wright St. Champaign, IL 61820-6242			8. PERFORMING ORGANIZATION REPORT NUMBER:	
9. SPONSORING/MONITORING AGENCY NAME(S) AND ADDRESS(ES) AFOSR - NE 110 Duncan Avenue, Suite B115 Bolling AFB, DC 20332-0001			10. SPONSORING/MONITORING AGENCY REPORT NUMBER: F49620-95-1-0238	
11. SUPPLEMENTARY NOTES:				
12a. DISTRIBUTION AVAILABILITY STATEMENT Approved for public release; distribution unlimited.			12b. DISTRIBUTION CODE	
13. ABSTRACT (Maximum 200 words) This AFOSR-funded research program is directed towards the demonstration and development of compact sources of visible and ultraviolet radiation. One of the most significant accomplishments of the past two years is the demonstration of microdischarge devices fabricated in silicon. These devices are cylindrical in cross-section with diameters <400 μ m, lengths of several mm, have specific power loadings >500 W-cm ⁻² and are capable of operating at pressures above one atmosphere. Another highlight of this research effort is that the first fiber laser pumped by a red diode laser was demonstrated; a green Ho-doped fluoride glass fiber laser pumped by a 25 mW red diode laser has a pump power threshold <5 mW, the lowest for any visible fiber laser. Also, the ability of atomic wavepackets to produce coherent radiation in the UV was also demonstrated. The significance of these results is discussed.				
14. SUBJECT TERMS 19971002 011			15. NUMBER OF PAGES:	
			16. PRICE CODE	
17. SECURITY CLASSIFICATION OF REPORT: UNCLASSIFIED	18. SECURITY CLASSIFICATION OF THIS PAGE UNCLASSIFIED	19. SECURITY CLASSIFICATION OF ABSTRACT UNCLASSIFIED	20. LIMITATION OF ABSTRACT	

QUALITY INSPECTED

FINAL REPORT FOR
AFOSR GRANT F49620-95-1-0238

Prepared for

Dr. H. R. Schlossberg
Physics and Electronics Directorate
AFOSR/NE
Bolling AFB
Washington, DC 20032

Submitted by

J. G. Eden
Department of Electrical and Computer Engineering
University of Illinois
Urbana-Champaign Campus
1406 W. Green Street
Urbana, IL 61801

June 1997

TABLE OF CONTENTS

	Page
SUMMARY	1
I. INTRODUCTION	2
II. ACCOMPLISHMENTS REALIZED UNDER AFOSR F49620-95-1-0238 SUPPORT	3
A. Microdischarge Devices in Silicon	3
B. Rare Earth:ZBLAN Fiber Lasers	5
C. Planar Waveguides in Fluoride Glass and LiNbO_3	7
D. Stimulated Emission in GaN.....	8
E. Generation of Coherent UV Radiation by the Interaction of a Wavepacket With Four Wave Mixing.....	8
III. PUBLICATIONS RESULTING FROM AFOSR SUPPORT	9
IV. AWARDS RECEIVED (J. G. Eden)	10
V. GRADUATE STUDENTS SUPPORTED—DEGREES RECEIVED.....	10
VI. Ph.D. GRADUATES TO DATE	10
APPENDIX: RECENT REPRINTS	13

SUMMARY

Under grant no. F49620-95-1-0238, AFOSR has supported an experimental program at the University of Illinois that is directed towards the demonstration and development of compact sources of visible and ultraviolet (UV) radiation. Particular emphasis has been placed on fiber and planar waveguide oscillators and amplifiers and their utility in optical diagnostic or sensing applications. This program was a productive one as evidenced by the following accomplishments:

- 1) Discharge devices micromachined in silicon have been fabricated and operated in Ne and N₂ at pressures exceeding 500 Torr; these devices have apertures < 400 μ m and are sources of intense visible and UV radiation;
- 2) The rare earth-doped:ZBLAN fiber lasers are being developed into practical devices. The threshold pump power for the green Ho:ZBLAN fiber laser has been reduced below 6 mW and new UV and visible transitions of Nd³⁺ and Tm³⁺ in ZBLAN fiber have been observed. The Pr:ZBLAN fiber laser is being operated with an external cavity for the purpose of frequency-doubling into the UV;
- 3) Pumping of a fiber laser by a red semiconductor diode was demonstrated for the first time.
- 4) Working with another group at Illinois, a process for fabricating rare earth-doped fluoride glass films by sol-gel techniques has been developed; LiNbO₃ films grown by sol-gel processes are also being explored;
- 5) Stimulated emission at room temperature has been observed from GaN films grown at Illinois by plasma-assisted MBE utilizing a novel nitrogen discharge source; quantum well structures have also been grown and are under study;
- 6) Coherent UV radiation that is modulated at terahertz rates has been generated by atomic wavepackets; although this initial demonstration took place with a gas phase system, the use of wavepackets to generate ultrashort pulses of UV coherent radiation shows promise for solid state systems as well.

This report will describe each of these results in detail.

I. INTRODUCTION

For the past 2 years, AFOSR has supported through the Electronics and Physics Directorate a research program that is directed toward the demonstration, development and application of new, compact sources of visible and ultraviolet (UV) radiation. The intent is to combine recent advances in MEMS, fiber, and film growth technologies to produce a family of compact or micro-devices that are capable of being integrated into an electro-optical system containing, for example, EO-modulators and laser diodes. We are particularly interested in the applications of such devices in medical diagnostics, spectroscopic sensing (especially in the UV), reprographics, and stereolithography.

This research effort has two major thrusts, both of which have proven to be quite successful thus far:

- 1) MEMS technology has been adopted to fabricate microdischarge devices in silicon. Our present devices have apertures $\leq 400 \mu\text{m}$ in diameter and length-to-aperture ratios ranging from ~ 2 to >6 . Discharge geometries other than cylindrical will be pursued in the future but it is already clear that these are extremely interesting devices. Specific power loadings $>500 \text{ W-cm}^{-3}$ have been achieved on a CW basis. Furthermore, these devices operate stably at gas pressures $>500 \text{ Torr}$ and produce intense visible and UV emission when operated with neon or N_2 . A patent application has been filed on these developments.
- 2) The second major aspect of this program is the development of fiber and planar waveguide oscillators and amplifiers operating in the visible and UV. Based on upconversion in rare earth-doped glass or crystalline materials such as ZBLAN (fluorozirconate glass) or LiNbO_3 , these devices have proven to be remarkably efficient. In the past year, for example, the pump power threshold for the Ho:ZBLAN green fiber laser has been reduced to $< 6 \text{ mW}$ (launched, not absorbed!) which brings this device well within the power levels available from low power, single mode semiconductor lasers. Indeed, pumping of the Ho:ZBLAN laser with a red semiconductor diode laser was recently demonstrated in our laboratory. This is, to our knowledge, the first fiber laser pumped by a red laser diode. Also, this represents the lowest pump power threshold for *any* upconversion fiber laser. New, intense lines in the deep visible to mid-UV have been observed in Tm:ZBLAN and Nd:ZBLAN fibers pumped by novel 2 and 3 photon schemes. Perhaps more importantly, in collaboration with another group at Illinois, a sol-gel process for producing oxide glass films (and waveguides) and a gaseous technique for converting these films to *fluoride* glass have been developed.

In addition to these key results, we have also realized the following accomplishments under this AFOSR program:

- 3) Stimulated emission has been observed at room temperature from GaN films grown at Illinois by plasma-assisted MBE with a novel nitrogen plasma source. These results were obtained in collaboration with another research group in our department. Quantum well structures have also been grown and are presently under study.
- 4) Coherent radiation at discrete wavelengths in the UV has been generated by the interaction of an atomic wavepacket with four wave mixing. The UV emission is both spatially and temporally coherent and is modulated at THz rates by the wavepacket. The crucial role played by the wavepacket suggests the potential to shape the temporal behavior of the emission as well as to generate coherent THz radiation.

Each of the areas will be addressed in the following section.

II. ACCOMPLISHMENTS REALIZED UNDER AFOSR F49620-95-1-0238 SUPPORT

A. Microdischarge Devices in Silicon

By adopting processing techniques that are widely used in the semiconductor industry and MEMS research, we have fabricated microdischarge devices in silicon that have several interesting and useful properties. A simplified diagram of a cylindrical device is shown in Fig. 1. Discharge cavities $< 400\text{ }\mu\text{m}$ in diameter and up to $\sim 4.5\text{ mm}$ in length have been fabricated thus far and electrical contact to the device is made by metal (typically Ni/Cr) films: 1) at the entrance to the discharge cavity, and 2) at the rear surface of the Si wafer. These devices work well with both metallurgical grade Si (98.4% purity) or high resistivity ($\rho > 100\text{ }\Omega\text{-cm}$) material.

Although simple from a conceptual standpoint, these devices have several profound advantages over conventional discharges:

- 1) Their primary asset is that, for a given operating pressure, the physical dimensions of the discharge can be made comparable to or less than key characteristic lengths for the discharge such as the electron-neutral collisional mean free path. Consequently, the discharge can be operated as a hollow cathode at pressures considerably higher than those obtainable in conventional (macro) discharges. That is, the pressure (p) at which a hollow cathode discharge can be generated is governed by the relationship: $pd = \text{constant}$, where d is the cathode's internal diameter. Consequently, hollow cathode discharges for exciting ion lasers

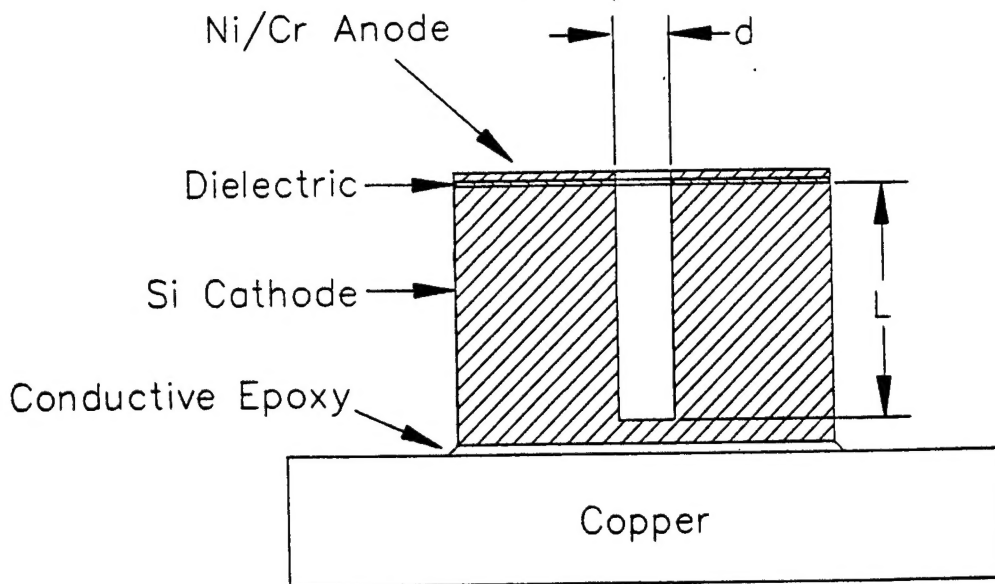


Fig. 1 Schematic diagram of a single microdischarge device fabricated in silicon. The dielectric in our initial experiments was a glass coverslip but SiO_2 or Si_3N_4 will work equally well.

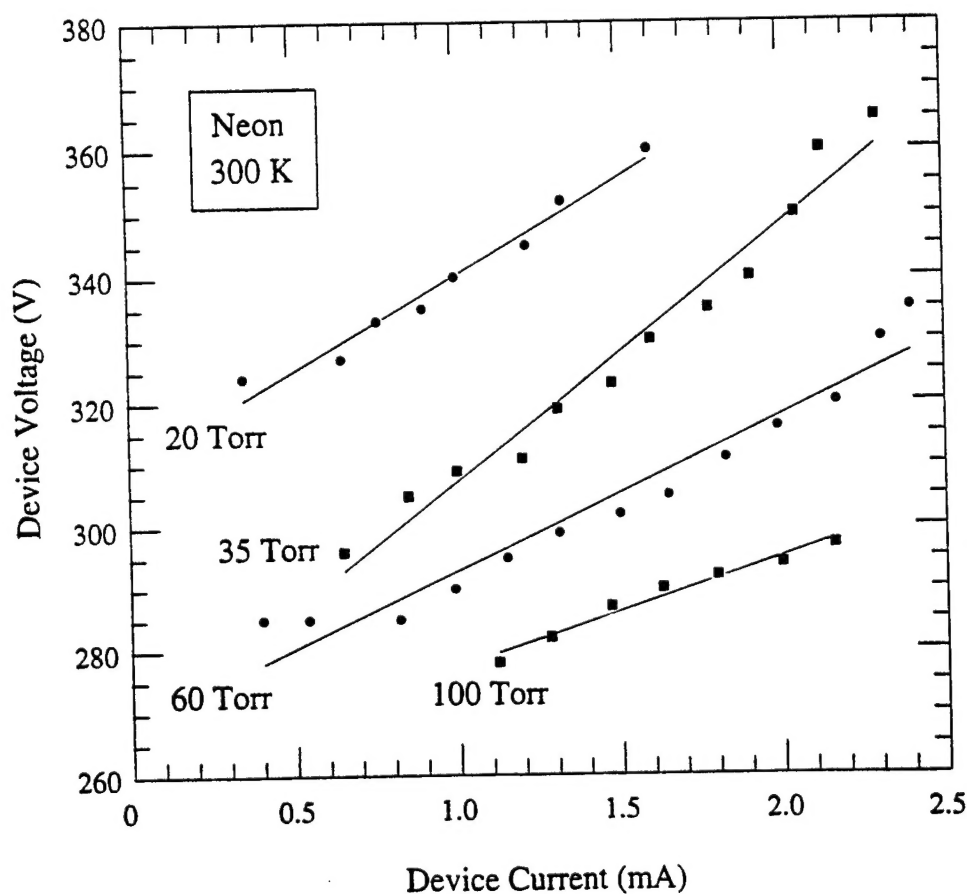


Fig. 2 Microcavity discharge I-V curves for a metallurgical grade Si device having a diameter of $400\ \mu\text{m}$ and a length of $1.75\ \text{mm}$. Data are shown for Ne pressures from 20 to 100 Torr.

and those in spectrophotometer lamps operate at pressures no greater than a few Torr whereas the devices discussed here operate at pressures beyond 500 Torr. The interest in a hollow cathode discharge is its characteristically high electron temperature. That is, the electrons are essentially ballistic, having acquired an energy roughly equivalent to the cathode fall potential.

- 2) It appears that the discharge can be operated as a hollow cathode discharge *or* a positive column by varying the discharge length (L)-to-diameter (d) ratio or the gas pressure. Therefore, the characteristics of the discharge can be altered for different applications.
- 3) The ability to produce miniature devices also has major implications for the design and manufacture of resonance lamps. Because the mean distance for the reabsorption of a mercury 253.7 nm resonance photon, for example, at a pressure of ~ 0.1 Torr is < 1 mm, commercial resonance lamps are constructed of capillary glass tubing and the effective radiating area is small. The other alternative is to decrease the number density of the metal vapor, thus allowing a corresponding increase in the discharge diameter. This is not a minor issue since resonance lamps (Hg and alkali vapor) are manufactured in this country for a wide range of applications, including germicidal treatments, polymer curing and lighting.

However, each microdischarge can be designed so that most resonance photons, regardless of where in the discharge they are produced, will escape and, hence, be useful. Furthermore, the Hg resonance line, for example, has a coherence length on the order of < 1 mm. Consequently, if the inter-discharge spacing in an array of devices is chosen properly, the entire discharge array will act as a phased array and the emitted radiation can be focused by a Fresnel lens.

- 4) An obvious attractive feature is the opportunity to adopt VLSI and MEMS processing techniques to fabricating large arrays. While our work has thus far investigated only two discharges on a chip, it appears that arrays of almost arbitrary size are quite feasible. Schoenbach et al.² have fabricated miniature discharge devices from molybdenum and mica insulators but utilizing silicon or glass is more attractive from a commercial and manufacturing standpoint.

Thus far, data have been acquired on more than a dozen devices and some of the results are summarized in Figs. 2 and 3. Experiments have been conducted with Ne and N₂ discharges and V-I characteristics for a Ne discharge having a ~ 400 μm diameter and a length of 1.75 mm are shown in Fig. 2 for pressures ranging from 20 to 100 Torr. Note that the slopes of the V-I curves are positive over the entire pressure range and that the specific power loading of the gas is > 500 W-cm⁻³. Stable operation of these devices has been obtained for pressures beyond 500

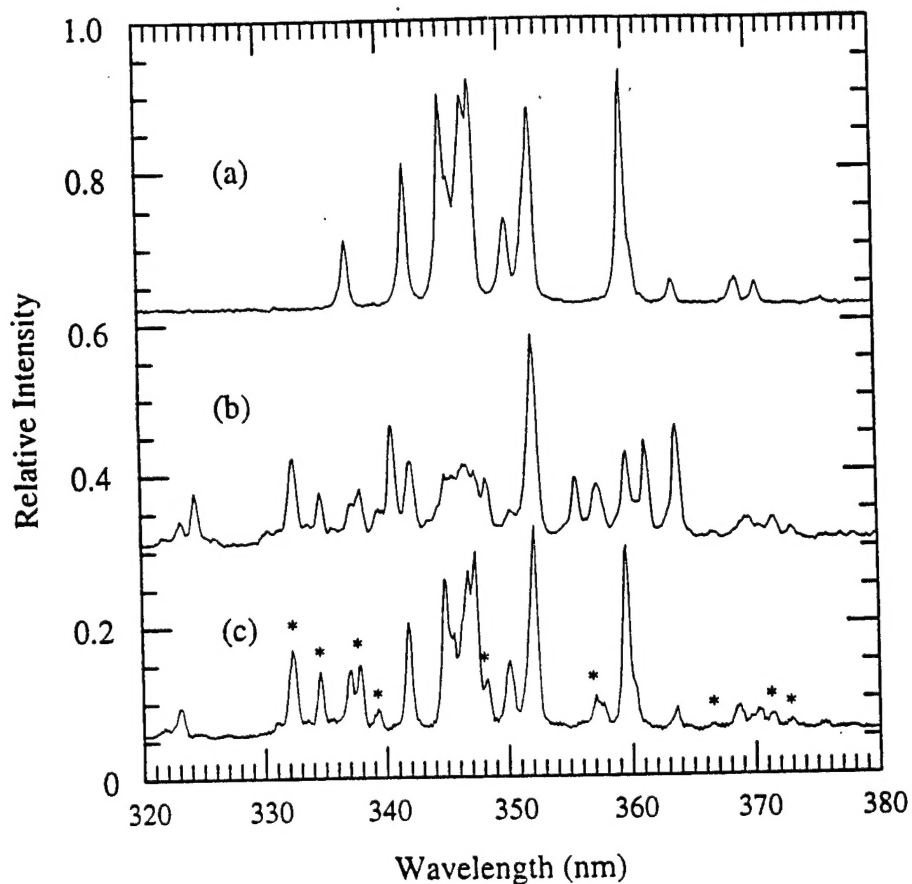


Fig. 3 Comparison of the Ne emission spectra in the near-UV (320-380 nm) produced by: a) a positive column ("pen lamp") discharge, b) a hollow cathode (spectrophotometer lamp) discharge, and c) a microdischarge device ($d = 400 \mu\text{m}$, $L = 3.5 \text{ mm}$) operating at 50 Torr, 235 V and 3.0 mA. The strongest Ne^+ lines are indicated by an asterisk in spectrum c).

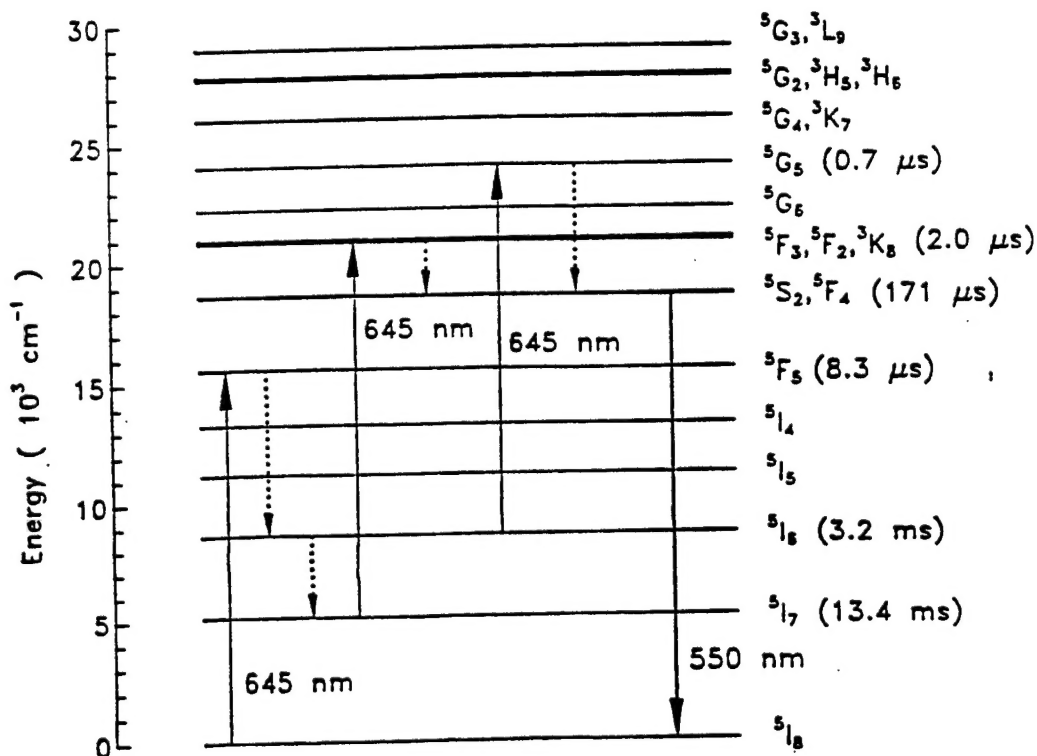


Fig. 4 Partial energy level diagram for Ho^{3+} in ZBLAN glass illustrating excitation of the 5S_2 state in the red.

Torr which suggests the potential for obtaining efficient CW emission from *molecular* species such as the rare gas dimers.

Spectroscopic experiments have also begun and we are especially interested in the performance of the device as the L/d ratio and pressure are varied. Figure 3 is a comparison of the Ne emission spectra in the UV (320-380 nm) from a positive column (penlight capillary source) discharge, a spectrophotometer hollow cathode discharge, and a microdischarge operating at 50 Torr ($d = 400\text{ }\mu\text{m}$, $L = 3.5\text{ mm}$, 235 V, 3.0 mA). These spectra indicate that the microdischarge behaves as a hollow cathode at pressures beyond 50 Torr, or roughly an order of magnitude larger than those accessible with conventional discharge devices. Specifically, all of the lines present in the microdischarge spectrum arise from Ne and Ne^+ but the latter are present only in the hollow cathode (Fig. 3(b)) and microdischarge spectra. The strongest Ne^+ features (at 334.55 and 332.38 nm) are the result of transitions originating from 2P^0 and 2F^0 states of the ion which lie $> 30\text{ eV}$ above the Ne (2p^6) ground state. Consequently, these devices act as hollow cathode discharges at pressures at least an order of magnitude larger than those accessible with a conventional discharge.

The performance of these devices and, in particular, the high operating pressures that are accessible, the positive V-I characteristic, and the opportunity to fabricate large planar arrays by VLSI and MEMS techniques show them to be very interesting from both scientific and applications perspectives. In particular, the ability to integrate Si microdischarge devices with photodetectors and control electronics offers tremendous device possibilities including sensors and atomic clocks. Because of the latter, a patent disclosure has been filed by the University of Illinois. Also, a manuscript describing the experimental results in more detail has been submitted to *Applied Physics Letters*.

B. Rare Earth:ZBLAN Fiber Lasers

A key part of this research program has been the pursuit of fiber and planar waveguide devices in the visible and UV based on upconversion in rare earth-doped fluoride glass or crystalline fibers and films. Although the sequential absorption of two or more pump photons is required to generate the desired visible or UV wavelengths, the rare earth-doped fluorozirconate glass (ZBLAN) fiber lasers have proven to be remarkably efficient and, through a systematic study of these devices, we continue to see major improvements in their performance.

One example is the Ho:ZBLAN upconversion fiber laser that operates in the red and green. Through steady improvements in fiber polishing and mounting procedures and spectroscopic measurements (gain, absorption, etc.) as a function of fiber length, NA, and core diameter, the performance of the green laser has steadily risen. The Ho:ZBLAN green line (λ

~549 nm) can be pumped in the visible and near-IR and Fig. 4 is a partial energy level for the Ho^{3+} ion in ZBLAN glass showing pumping of the $^5\text{S}_2$ state by the sequential absorption of two red (645 nm) photons. In recent experiments, we have demonstrated pump power thresholds below 6 mW (launched) for this laser. The variation of threshold pumping power with pump wavelength for a $\text{Ho}:\text{ZBLAN}$ fiber laser 22 cm in length is presented in Fig. 5. These data were obtained with a fiber having a core diameter of 1.7 μm and an NA of 0.39. Note that the pump power threshold is ≤ 6 mW (10 mW incident) over at least a 6 nm region (644-650 nm). These results represent the lowest thresholds (by almost a factor of 3) for any upconversion fiber laser and demonstrate that pumping of this laser is now well within the capabilities of commercially available, low power (15-30 mW), single mode, red semiconductor lasers. Indeed, in recent experiments, the senior graduate student on this program (Dave Funk) succeeded in pumping the $\text{Ho}:\text{ZBLAN}$ laser with a 25 mW red (643 nm) semiconductor diode laser. The threshold pump power was ~5 mW and > 1 mW was obtained in the green for 25 mW of pump power.

Both the output and tuning characteristics of this laser have also been examined and Fig. 6 shows that this oscillator will operate with cavity output couplings as large as 96% (Fresnel reflection from one end of the fiber). The slope efficiency for this short laser (27.5 cm) is 4.5% and we expect that value to rise with further improvements in fiber preparation, mirror mounting and the use of newer fiber that is now available. Also, as illustrated in Fig. 7, this laser has been tuned over more than 10 nm in the green. Tuning is nearly continuous although Fig. 7 shows the results obtained at a few discrete wavelengths. Details concerning the tuning behavior of this laser can be found in one of the reprints in the Appendix.

Similar experiments are underway with the $\text{Pr}:\text{ZBLAN}$ fiber laser in which our primary interest is the red (635 nm) and orange (617 nm) lines as candidates for frequency-doubling. Our fibers are co-doped with Yb to allow for pumping of the laser in the ~800-925 nm region. Several groups have explored this laser as a potential white light laser and have observed slope efficiencies and output powers for the red line exceeding 50% and 300 mW, respectively. Our primary interest is in developing a fiber laser widely tunable in the UV. Recent experiments in our laboratory have focused on identifying and pumping higher-lying Re^{3+} excited states that may be suitable as upper levels for UV and deep-visible lasers. Excited states lying above ~30,000 cm^{-1} are not well known for several of the rare earth ions and spectroscopic experiments conducted in our laboratory have identified pumping schemes for Tm^{3+} and $\text{Nd}^{3+}:\text{ZBLAN}$ that efficiently excite both UV and visible lines. Considering $\text{Nd}:\text{ZBLAN}$, for example, Fig. 8 illustrates two schemes that have been identified for pumping the $^2\text{F}(2)_{5/2}$ state of Nd^{3+} at ~38,000 cm^{-1} . One or two color excitation schemes produce intense visible and near-UV fluorescence at wavelengths ranging from 390 to 530 nm (cf. Fig. 9). Notice that all of the

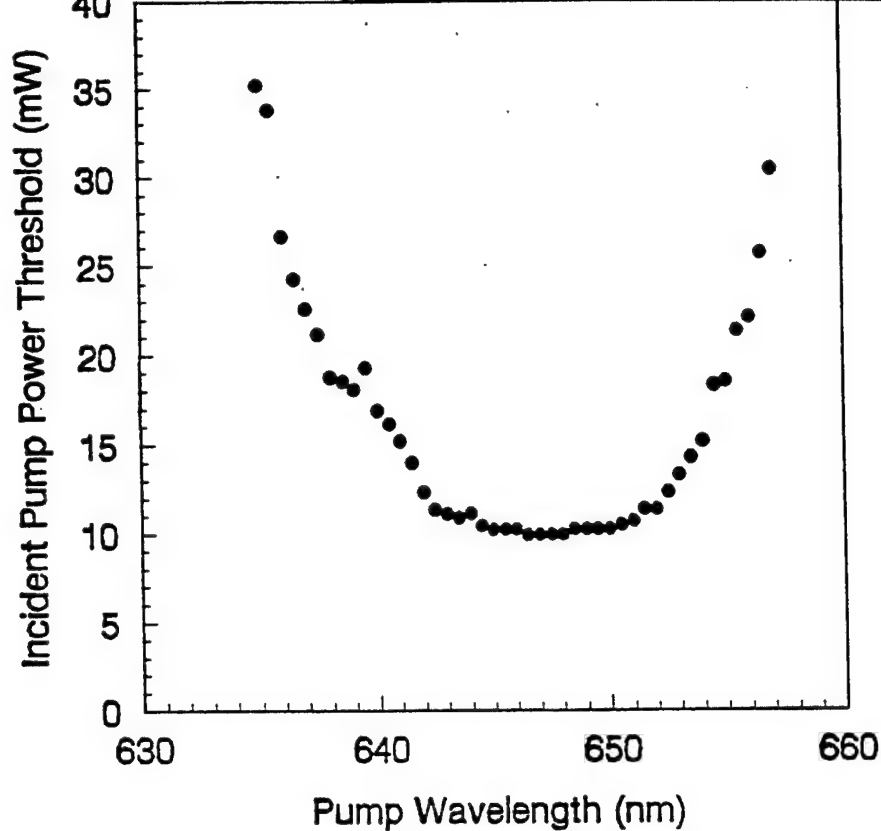


Fig. 5 Dependence of threshold pump power on pump wavelength for Ho:ZBLAN fiber lasers 22 cm in length. The fiber has a core diameter of $1.7\ \mu\text{m}$ and a NA of 0.39. Note that the ordinate gives pump power incident on the input coupling optics. The launching efficiency is $< 60\%$.

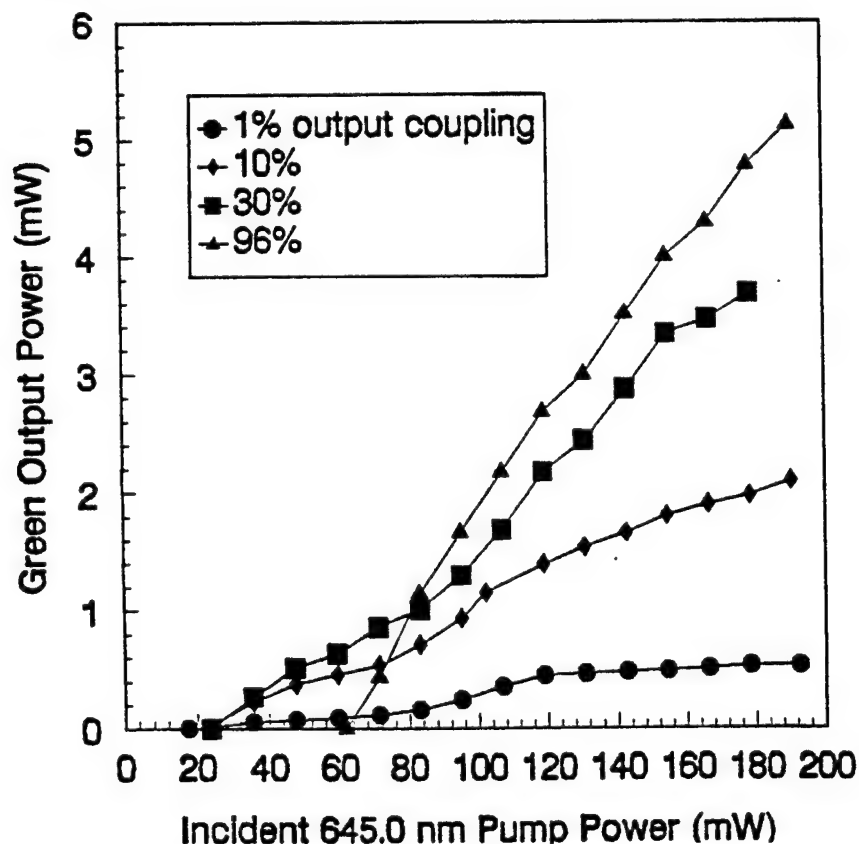


Fig. 6 Output power as a function of input power for the green Ho:ZBLAN fiber laser. The results are for various cavity output couplings, a fiber length of 27.5 cm and a core diameter of $3\ \mu\text{m}$.

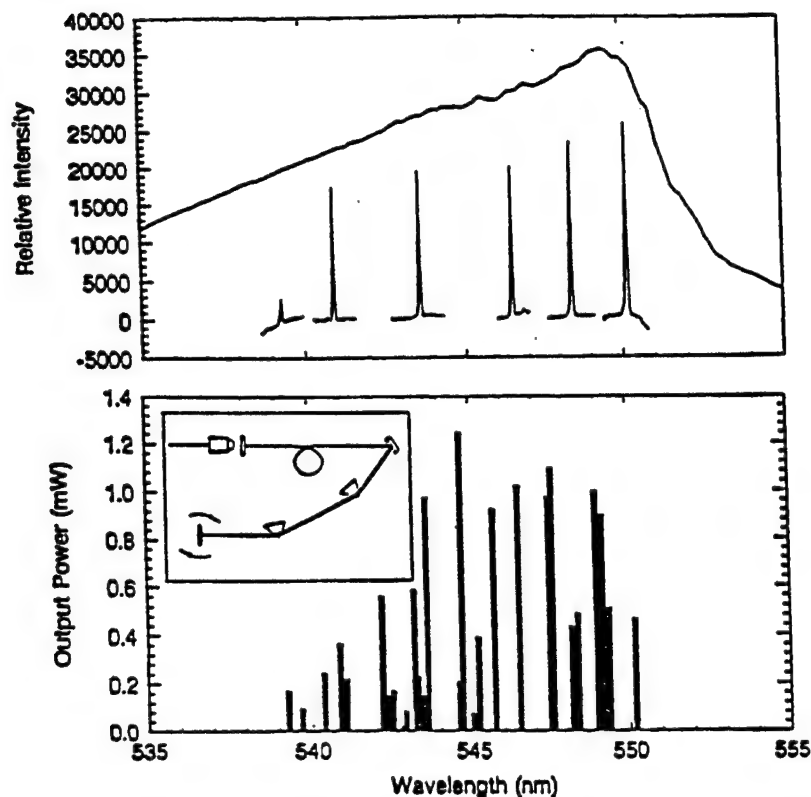


Fig. 7 Tuning data for the Ho:ZBLAN fiber laser. Tuning was accomplished with two intracavity prisms. The top portion of the figure shows the spontaneous emission spectrum for the transition and laser spectral lineshapes for operation at several discrete wavelengths. The bottom figure shows the variation of output power with laser wavelength for a high-Q resonator.

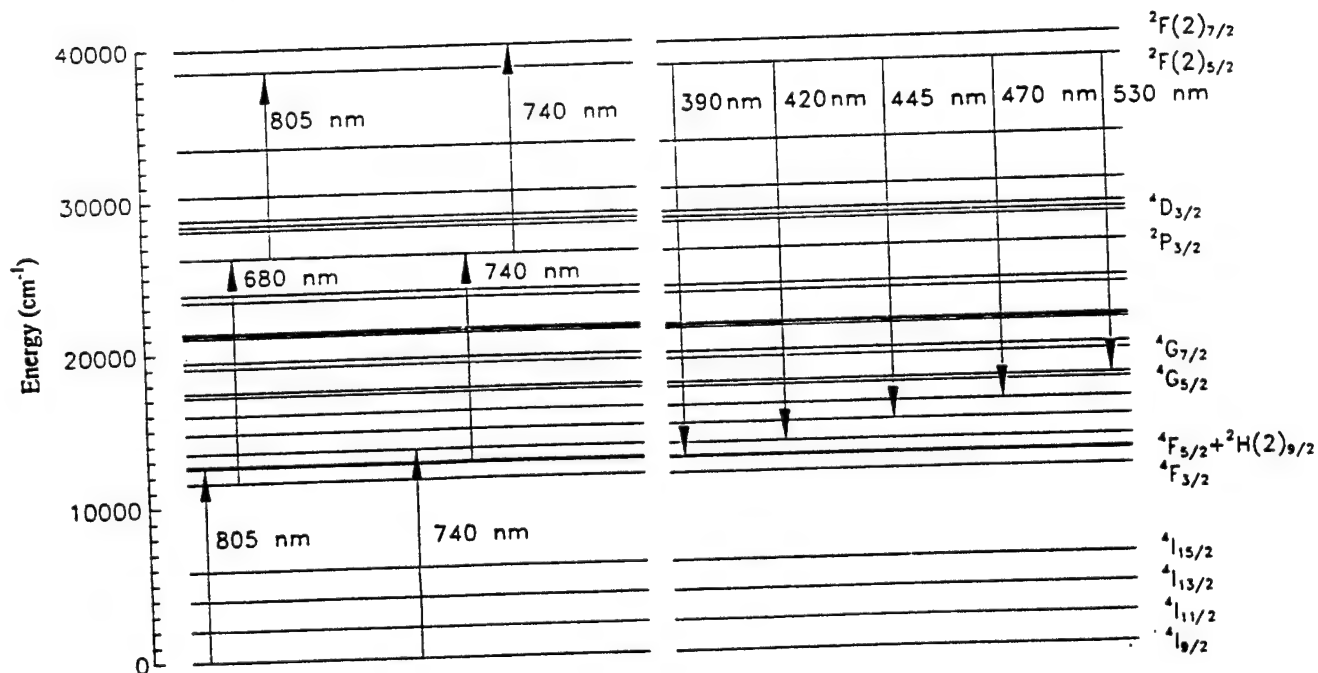


Fig. 8 Partial energy level diagram of Nd^{3+} illustrating three photon excitation of the $2\text{F}(2)_{5/2}$ state and subsequent fluorescence in the near-UV and visible.

emission lines originate from the same excited state and that, when pumping at 740 nm, the pump not only populates the upper laser level but also depletes the $^4F_{5/2}$ state population. Attempts to obtain lasing on these transitions in Nd:ZBLAN fiber is underway and similar pumping pathways have been developed for Tm^{3+} . In the latter case, strong transitions in the mid-UV are also excited.

C. Planar Waveguides in Fluoride Glass and $LiNbO_3$

In collaboration with another research group at the University of Illinois and several individuals at NIST in Boulder, CO, we have been pursuing the development of active planar waveguides operating in the visible or UV. Although fiber lasers have shown the potential for upconversion-based active devices, the cylindrical geometry of the fiber is not optimal for several applications (such as optical data storage), and particularly in those situations in which on-chip integration with a photodetector, modulator, or other device is desired. Consequently, the focus of this phase of our research program has been the growth of rare earth-doped fluoride glass and crystalline films by one of several growth techniques and the fabrication of visible- (or UV-) active devices from these films.

Our efforts are currently centered on the deposition of heavy metal-fluoride glass by sol-gel processes. Professor David Payne of the Department of Materials Science at the University of Illinois and his students have years of experience in sol-gel processing and, for example, were the first to integrate GaAs and $PbTiO_3$ by sol-gel techniques. Also, his group has perfected the sol-gel growth of patterned $LiNbO_3$ films that are well-suited as periodically-poled devices for frequency conversion but our primary attention is devoted to fabricating fluoride glass films suitable for optical waveguides. Producing La-based fluoride glass films by sol-gel processing requires two steps that our groups working together have demonstrated successfully. The first phase entails depositing oxide glass films from a suitable metal alkoxide precursor; subsequently, the oxide glass is converted to its fluoride counterpart by a liquid or gas phase process. Approximately one year ago, we were successful in converting oxide glass films to fluoride glass by a liquid process but the optical quality of the films was not acceptable for device applications. In more recent work, however, the conversion to fluoride glass has been demonstrated successfully in our laboratory by an HF (gas phase) process and, although their optical characteristics have not yet been quantified, these films appear to be of good quality. The data of Fig. 10 demonstrate that the conversion of the oxide film to the fluoride glass has been accomplished. The top portion of the figure shows the absorption spectrum in the mid-IR (~ 1000 - 4000 cm^{-1}) of a La-oxide glass film grown by a sol-gel process. After processing the film with HF, the oxide features at ~ 1600 and 3300 cm^{-1} have vanished (bottom of Fig. 10). In

Fluorescence Spectra of Nd^{3+} :ZBLAN Fiber
Pumped by 580 mW @ 729.8 nm

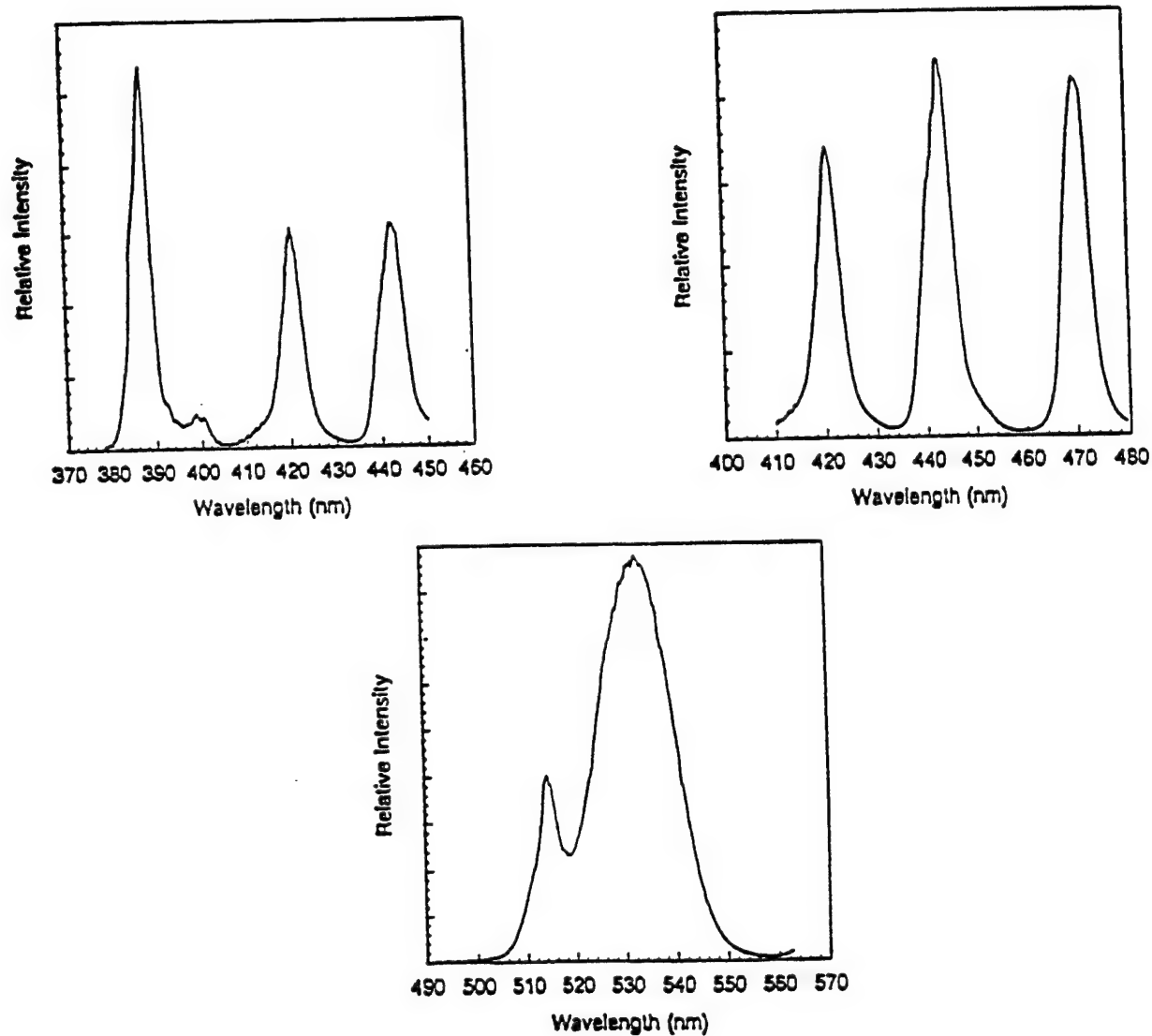


Fig. 9 Emission spectra observed from Nd:ZBLAN fiber when pumping the $^2\text{F}(2)_{5/2}$ state at 740 nm (cf. Fig. 8).

PERKIN ELMER

94.89
%T

0.07

4000 3500 3000 2500 2000 1500 1000 500 cm^{-1}

93.67
%T

4.05

4000 3500 3000 2500 2000 1500 1000 500 cm^{-1}

Fig. 10 Transmission spectra in the $\sim 2.5\text{-}10\ \mu\text{m}$ region in the infrared for La-bearing glass films grown in CaF_2 by sol-gel processing. The top trace is an oxide film showing characteristic features at ~ 3300 and $\sim 1600\ \text{cm}^{-1}$. The lower trace is that observed after the film was converted to its fluoride counterpart by processing with HF .

these experiments, the films were grown on CaF_2 substrates. We consider this to be a significant accomplishment since, to our knowledge, no other process has yet been demonstrated for producing high quality, heavy metal-fluoride glass films by sol-gel processing.

D. Stimulated Emission in GaN

Collaborations with a second group at Illinois have also contributed significantly to this research effort. Professor Kevin Kim of the Department of Electrical and Computer Engineering is an expert in thin film growth by MBE and cluster beam techniques and his group has grown low loss silica waveguides by cluster beam techniques. Recently, we have obtained stimulated emission from $\sim 1 \mu\text{m}$ thick GaN films grown on basal plane sapphire at 750°C by plasma-assisted MBE. The plasma-source is a novel inductively-coupled discharge in which the plasma is electrostatically confined within a boron nitride tube. The result is high quality GaN films which, when studied by photoluminescence at 325 nm (He-Cd laser), yielded only the GaN exciton peak at 364 nm with a spectral width at 300 K of 8 nm (75 meV).

These films exhibit strong stimulated emission at room temperature when optically pumped at 355 nm. Figure 11 illustrates the spectra recorded when the films are pumped in vertical geometry with intensities ranging from $3\text{--}8 \text{ MW}\cdot\text{cm}^{-2}$. A sharp increase in the wavelength-integrated emission intensity occurs for $I_p \gtrsim 4 \text{ MW}\cdot\text{cm}^{-2}$. Note, too, that the FWHM of the spectrum falls by more than a factor of two when I_p is increased from ~ 4.1 to $4.7 \text{ MW}\cdot\text{cm}^{-2}$. These results were published in a recent issue of *Applied Physics Letters*.

Quantum well structures have also been grown with this system and are currently under study.

E. Generation of Coherent UV Radiation by the Interaction of a Wavepacket With Four Wave Mixing

For approximately the past two years, our laboratory has been investigating nonlinear techniques for efficiently generating coherent UV or VUV radiation. We have recently demonstrated that pulsed coherent UV radiation can be produced when an atomic wavepacket (produced by an initial "pump" pulse) interacts via four wave mixing with an intense optical field. In these experiments, ns and $(n-2)d$ states of Rb ($n = 10\text{--}12$) are excited by two photon transitions in the red with ~ 100 fs, $50 \mu\text{J}$ pulses provided by a CPM/4 stage amplifier system. Since several Rb excited states are driven coherently by the pump pulse, a wavepacket is formed. When a second red pulse arrives, UV emission is produced near the $m^p 2P_{3/2} \rightarrow 2S_{1/2}$ (ground) ($m = 7\text{--}11$) resonance transitions of the atom and calculations show clearly that all of the key features of the spectrum are explained by axially phase-matched, four wave mixing. Also, one is

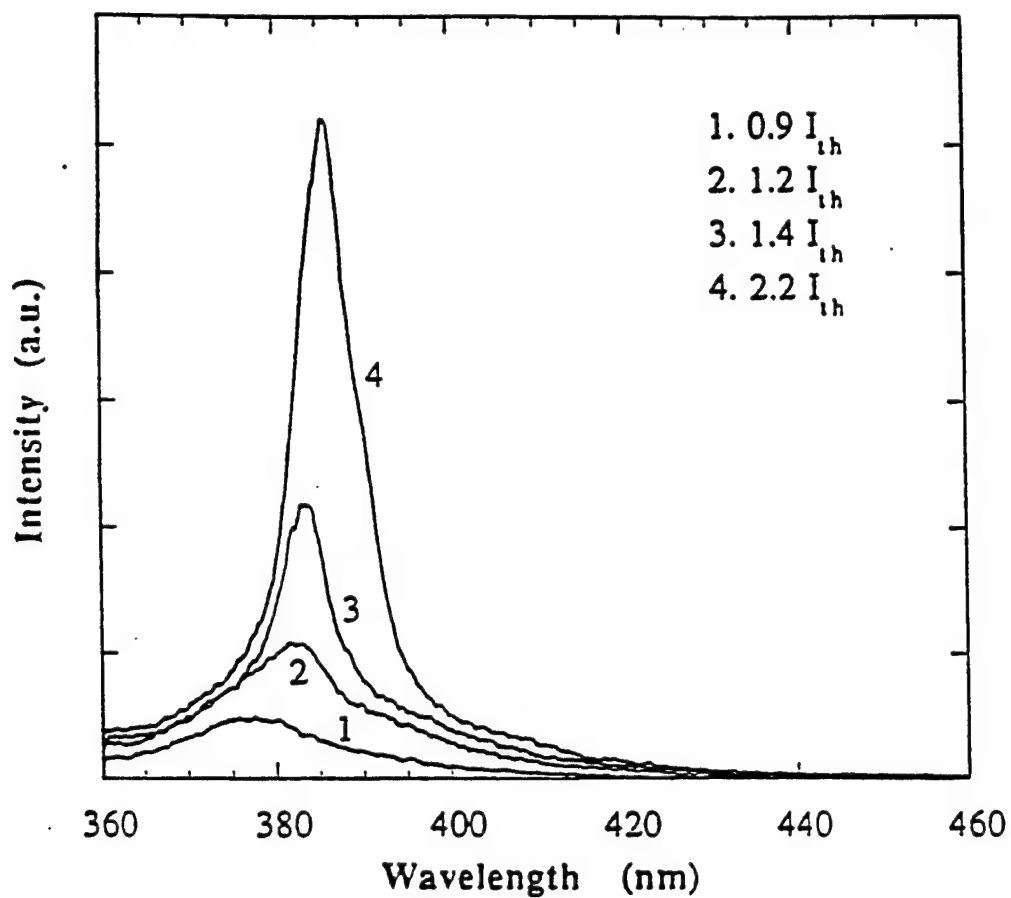


Fig. 11 GaN emission spectra recorded for four values of pumping intensity ($I_{th} = 3.6$ MW-cm⁻²; $\lambda_p = 355$ nm). Spectral narrowing is evident for pumping intensities $> I_{th}$ and the spectral width falls by more than a factor of two in the $4 \leq I_p \leq 4.7$ MW-cm⁻² interval.

able to monitor the temporal history of the wavepacket by recording the relative intensity of the UV emission as the time delay between the pump and probe pulses is varied. Figure 12 shows that the oscillatory behavior expected for a wavepacket is observed; the ~ 350 fs observed periodicity is precisely what one would expect if the dominant contribution to the wavepacket arises from quantum beating between the 11s and 9d states ($11s-9d \cong 94 \text{ cm}^{-1}$).

To summarize, we believe these results to be extremely significant since:

- 1) The optical detection of a wavepacket has been demonstrated for the first time;
- 2) Spatially and temporally coherent UV emission has been generated by the interaction of a wavepacket and an intense, ultrashort visible laser pulse by four wave mixing.
- 3) The interaction of the wavepacket and four wave mixing modulates the UV at terahertz rates.
- 4) This technique should be applicable to other vapor phase *and* doped solid state systems to generate subpicosecond coherent UV radiation.

III. PUBLICATIONS RESULTING THUS FAR FROM AFOSR F49620-95-1-0238 SUPPORT

1. R. B. Jones, H. C. Tran, and J. G. Eden, "Photoabsorption of Kr_2^+ in the ultraviolet: Revisited," *J. Chem. Phys.* **102**, 4329 (1995).
2. D. S. Funk, J. W. Carlson, and J. G. Eden, "Room temperature fluorozirconate glass fiber laser in the violet (412 nm)," *Opt. Lett.* **20**, 1474 (1995).
3. G. Rodriguez, P. C. John, and J. G. Eden, "Vibrational wave packets in the $\text{C } ^1\Pi_u$ state of Cs_2 : Two color pump-probe experiments," *J. Chem. Phys.* **103**, 10473 (1995).
4. D. S. Funk, S. B. Stevens, S. S. Wu, and J. G. Eden, "Tuning, temporal, and spectral characteristics of the green ($\lambda \sim 549 \text{ nm}$), holmium-doped fluorozirconate glass fiber laser," *J. Quantum Electron.* **32**, 638 (1996).
5. G. Rodriguez, C. M. Herring, R. D. Fraser, and J. G. Eden, "Photodissociation of PbI_2 in the ultraviolet: Analysis of the $A \rightarrow X$ band of PbI ," *J. Opt. Soc. Am* **13**, 1362 (1996).
6. D. S. Funk and J. G. Eden, "Upconversion fiber lasers operating in the visible and ultraviolet," *Proc. SPIE* **2841**, 42-49 (1996).
7. H. C. Tran, P. C. John, J. Gao, and J. G. Eden, "Interaction of atomic wavepackets with four wave mixing: Detection of rubidium and potassium wavepackets by coherent ultraviolet emission," (submitted to *Opt. Lett.*).
8. J. W. Frame, D. W. Wheeler, T. A. DeTemple, and J. G. Eden, "Microdischarge devices in silicon," (submitted by *Appl. Phys. Lett.*).

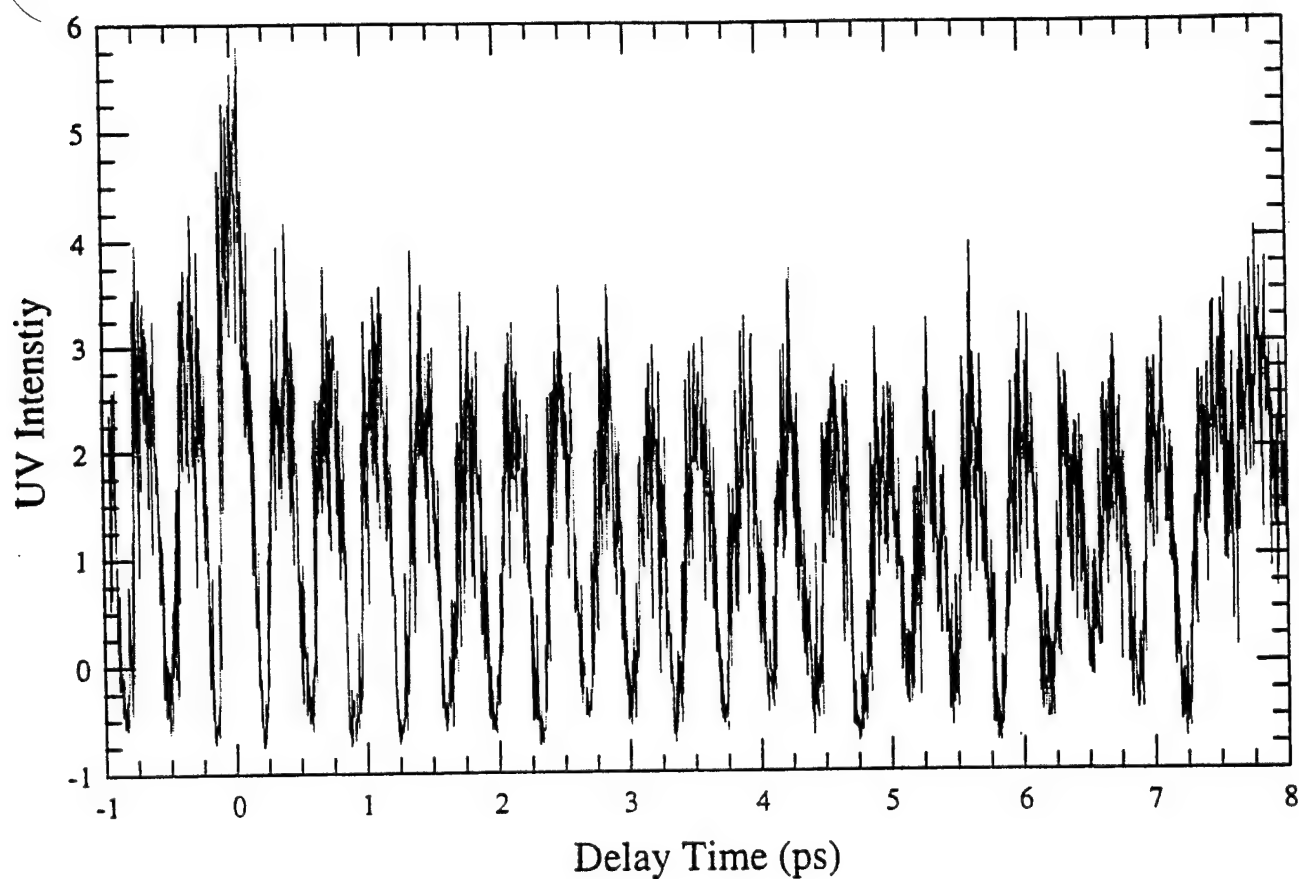


Fig. 12 Variation of the UV intensity produced near the $10p\ ^2P_{3/2} \rightarrow 5s\ ^2S_{1/2}$ transition when the time delay Δt between two red ($\lambda \simeq 620\text{ nm}$), $\sim 100\text{ fs}$ pulses is scanned. The periodicity of the signal is $\sim 350\text{ fs}$ which is precisely what one would expect for quantum beating between the $11s$ and $9d$ states of Rb.

Several other manuscripts describing our results on microdischarge devices, the Ho:ZBLAN laser pumped by a red semiconductor laser, and wavepacket experiments are in preparation.

IV. AWARDS RECEIVED (**J. G. Eden**)

Distinguished Service Award, IEEE Lasers and Electro-Optics Society, 1996
James F. Towey University Scholar, UIUC, 1996-98

V. GRADUATE STUDENTS SUPPORTED — DEGREES RECEIVED

Cyrus M. Herring, Electrical and Computer Engineering (requirements for Ph.D. degree completed in June 1997).

James J. Alwan, Electrical and Computer Engineering (Ph.D. degree received — presently employed at Micron Technology).

Hao C. Tran, Physics (Ph.D. degree received — presently employed at Northrop Grumman).

Z. Gurkan Figen, Electrical and Computer Engineering.

Ju Gao, Electrical and Computer Engineering.

David J. Wheeler, Electrical and Computer Engineering (M.S. degree to be awarded in late 1997).

VI. Ph. D. GRADUATES TO DATE

The following list gives the names, year of graduation, first (and, in several cases, second) employer, and area of work for each of the individuals that have received the Ph.D. degree (in Electrical and Computer Engineering or Physics) under the direction of Prof. Eden.

M. L. Dlabal (1981) – Naval Research Laboratory (Phase Conjugation, Beam Cleanup, Excimer Lasers) – Electrical and Computer Engineering.

A. W. McCown (1983) – Los Alamos National Laboratory (KrF Lasers, Gas Laser Kinetics) – Physics.

J. F. Osmundsen (1984) – Rockwell International, University of California-San Diego (Non-Linear Phenomena, Beam Cleanup) – Electrical and Computer Engineering.

D. E. Johnson (1985) – Phillips Laboratory, Kirtland AFB (Chemical Excimer Lasers) – Physics.

M. N. Ediger (1985) – Naval Research Laboratory, FDA (Biological Applications of Lasers and Molecular Spectroscopy) – Electrical and Computer Engineering.

K. P. Killeen (1985) – Sandia National Laboratory, Hewlett-Packard (Laser Growth of Semiconductor Films, MOCVD) – Electrical and Computer Engineering.

D. P. Greene (1985) – Los Alamos National Laboratory (Excimer Lasers, Optics) – Electrical and Computer Engineering.

D. B. Geohegan (1986) – Oak Ridge National Laboratory (Growth of Films by Laser Ablation, Laser Diagnostics) – Physics.

D. J. Kane (1989) – Los Alamos National Laboratory, Southwest Sciences, Inc. (Femtosecond Laser Spectroscopy) – Physics.

C. C. Abele (1989) – Questek Corp., Cynosure, General Scanning (Rare Gas-Halide and Dye Laser Development for Medical Applications) – Electrical and Computer Engineering.

D. C. Shannon (1989) – Lightwave Electronics Corp., Acculight, Inc. (Development of Diode-Pumped Solid State Lasers) – Electrical and Computer Engineering.

J. H. Schloss (1989) – Lawrence Livermore National Laboratory, Marsh, Inc., SSI Technologies (Solid State Laser Materials, Optical Sensors) – Electrical and Computer Engineering.

K. K. King (1989) – Ohio State University, Potomac Photonics, Marsh, Inc. (Laser Materials Processing) – Physics.

S. B. Kim (1991) – California Institute of Technology (Chemistry, Femtosecond Spectroscopy) – Electrical and Computer Engineering.

C. J. Zietkiewicz (1991) – Helios, Inc., Melles-Griot (Infrared Gas Lasers, Optics) – Electrical and Computer Engineering.

R. B. Jones (1992) – Oak Ridge National Laboratory, Northrop Corp. (Laser Spectroscopy of Biological Molecules, Solid State Lasers) – Electrical and Computer Engineering.

G. Rodriguez (1992) – Los Alamos National Laboratory (Femtosecond Spectroscopy and Chemical Kinetics) – Electrical and Computer Engineering.

Y. Y. Gu (1993) – University of Illinois (Laser Remote Sensing of the Atmosphere) – Electrical and Computer Engineering.

A. M. Farkas (1994) – Cornell University (Environmental and Combustion Applications of Laser Spectroscopy) – Electrical and Computer Engineering.

J. J. Alwan (1995) – Micron Technology (Display Panel Technology) – Electrical and Computer Engineering.

R. D. Fraser (1995) – Resonetics, Siemens Medical Systems (Micromachining of Materials with Excimer Lasers) – Electrical and Computer Engineering.

H. C. Tran (1995) – Northrop Corp. (Infrared OPOs, Solid State Lasers) – Physics.

P. C. John (1996) – Lockheed-Martin Corp. (Gas Lasers, Optical Systems) – Electrical and Computer Engineering.

C. M. Herring (1997) – University of Illinois (Ultrafast and Molecular Spectroscopy) – Electrical and Computer Engineering.

APPENDIX:
RECENT REPRINTS

Tuning, Temporal, and Spectral Characteristics of the Green ($\lambda \sim 549$ nm), Holmium-Doped Fluorozirconate Glass Fiber Laser

David S. Funk, S. B. Stevens, S. S. Wu, and J. Gary Eden, *Fellow, IEEE*

Abstract—The output power, tuning and temporal behavior of the green (539–550 nm), Ho-doped fluoro-zirconate glass (ZBLAN) fiber laser pumped in the red ($\lambda \sim 643$ nm) has been examined in detail. Fibers ranging in length from ~ 20 –86 cm have been studied, and more than 38 mW of output power has been obtained from a 21 cm long fiber for 30% output coupling and 280 mW of absorbed pump power. By inserting two prisms into the optical cavity, the oscillator has been tuned over ~ 11 nm, and the emission spectrum of the free-running laser has been recorded as a function of pump power at both room temperature and 77 K. The self-pulsing (spiking) behavior of the laser and the influence of depletion of the Ho^{3+} ground state ($^5\text{I}_8$) population on the emission spectrum and efficiency of this system are discussed.

I. INTRODUCTION

COMPACT sources of CW coherent radiation in the visible and ultraviolet (UV) are few in number and, until recently, virtually all of the commercially available systems were gas lasers. In the green and blue portion of the spectrum, the choices have been limited primarily to the He-Ne green transition (543.4 nm), Ar ion (458–514 nm), and He-Cd (442 nm). The dominance of gas lasers at these wavelengths for more than three decades is both remarkable and a testimony to the simplicity of gaseous systems, their excellent beam quality and the steady improvement of device performance (size reduction, new wavelengths, enhanced power, and lifetime) through engineering.

Although their longevity and adaptability continue to surpass expectations, gas lasers suffer from several well-known drawbacks including excessive power consumption and physical size and solid-state alternatives are being aggressively pursued. One promising class of UV, visible, and near-infrared lasers that has emerged over the past several years is the upconversion fiber laser. Based on rare earth-doped fluoro-zirconate glass (ZBLAN) fibers, this family of lasers was discovered in 1990 [1], [2] and offers power outputs in the red (635 nm) and blue (480 nm) exceeding 100 mW and overall efficiencies

(pump-to-output) of ~ 10 –15%.¹ Lasing in the UV and violet from Nd-doped ZBLAN fibers was recently reported [3], [4], and the available wavelengths now span the 380 nm to > 2 μm region. The properties of these lasers have been described in more detail in [5].

The Ho:ZBLAN fiber laser operates in the infrared (1.2 and 2.0 μm), red (750 nm), and green ($\lambda \sim 549$ nm) and was the second of the visible upconversion fiber lasers to be demonstrated [2]. Although the green transition has been successfully pumped in the near-infrared (750 or 890 nm) [6], it is most efficient when pumped in the red (640–645 nm), and output powers > 12 mW were reported in [2], [7], and [8]. Lasing on the green transition of Ho^{3+} had previously been obtained by Voron'ko *et al.* [9] and Johnson and Guggenheim [10] in Ho-doped CaF_2 and BaY_2F_8 bulk crystals, respectively, but in both cases, it was necessary to cool the crystals to 77 K. While it is perhaps not as well-studied as other upconversion fiber lasers, Ho:ZBLAN is known to be widely tunable and exhibits one of the highest slope efficiencies reported to date (36%, [7]). In this paper, the results of a series of experiments in which the temporal and spectral behavior of the Ho:ZBLAN fiber laser were characterized [11] are described.

II. EXPERIMENTAL APPARATUS

The fibers for these experiments were fabricated from ZBLAN glass and have a Ho^{3+} concentration in the core of 1000 ppm molar and a NA of 0.15. Because the core and cladding diameters are 11 and 125 μm , respectively, the fiber is multimode at both the pump and laser wavelengths. Nineteen LP modes are propagating at 643 nm and more than 24 modes at 547 nm. Fiber lengths between 19.5 and 86 cm have been studied thus far, and virtually all of the experiments described here were carried out at room temperature.

Pumping of the fiber is provided by an Ar^+ laser-pumped, scanning ring dye laser having a linewidth (without etalons) of 20 GHz (~ 0.7 cm^{-1}) and operating in the red (630–690 nm). For all of the “free-running” (untuned) oscillator experiments,

¹In the literature, efficiencies of upconversion fiber lasers are specified in several ways. Since the efficiency with which pump power is launched into the fiber is dependent upon the NA and core diameter of the fiber as well as the input (coupling) optics, laser efficiency is often normalized to the launched power. By this definition, efficiencies have approached 40%. Also, slope efficiencies for several upconversion fiber lasers (such as Er (544 nm) and Tm (480 nm)) have exceeded 50% (cf. [5]). Most of the efficiencies reported here are referenced to the pump power absorbed by the fiber.

Manuscript received August 30, 1995; revised December 1, 1995. This work was supported by the U. S. Air Force Office of Scientific Research (H. R. Schlossberg).

The authors are with the Everitt Laboratory, Department of Electrical and Computer Engineering, University of Illinois, Urbana, IL 61801 USA.
Publisher Item Identifier S 0018-9197(96)02558-4.

the optical cavity was formed by butt coupling the polished ends of the fiber against two flat mirrors. One was a dichroic mirror having maximum transmission ($>95\%$) at 650 nm but a reflectivity $>99.9\%$ at 550 nm. It was through this mirror that the pump beam was launched into the fiber by means of a $10\times$ microscope objective. The estimated launching efficiency for this arrangement is $\sim 80\%$. One of five mirrors, having a transmission of 1.5, 3.1, 7.5, 11.6, or 31% at 550 nm, served as the output coupler for the optical cavity. Radiation emerging from the output coupler was collimated by a second $10\times$ microscope objective and passed through a 550 nm bandpass filter ($\Delta\lambda = 50$ nm FWHM). Power measurements were made with calibrated photoelectric or pyroelectric detectors and spectra were recorded by a diode array coupled to a 0.25 m spectrograph having a reciprocal dispersion (in first order) of 3.2 nm/mm. For 50 μm slits, the overall resolution of the detection system was ~ 0.2 nm in first order. Higher resolution scans of the laser spectrum were acquired with a 0.5 m Ebert spectrograph operating in second order. Laser waveforms were obtained with a Si photodiode and a digital signal analyzer having a bandwidth of 1 GHz.

Tuning of the oscillator was accomplished by installing two Brewster prisms and a concave mirror having a radius of curvature of 3 cm between the fiber and the output coupling mirror. The concave mirror served to collimate the radiation from the fiber, and the laser was tuned by rotating the output coupler.

III. RESULTS AND DISCUSSION

A. Excited State Kinetics, Multiphonon Relaxation

Fig. 1 is a partial energy level diagram for Ho^{3+} , showing the states relevant to the 549 nm upconversion laser. The absorption of a pump photon by the ground state ion ($^5\text{I}_8$) populates Stark sublevels of the $^5\text{F}_5$ excited state which subsequently relax nonradiatively (by multiphonon processes) to the lower-lying $^5\text{I}_6$ and $^5\text{I}_7$ levels. It has previously been shown [12]–[15] that the excited states of Ho^{3+} in fluorozirconate glass adhere to the phenomenological energy gap law which expresses the nonradiative decay rate for a given state as

$$W = C \exp(-\Delta E/a\hbar\omega), \quad (1)$$

where ΔE is the energy separation between the excited Ho^{3+} state of interest and the next lowest-lying level, C and a are constants, and $\hbar\omega$ is the highest energy phonon in the host (ZBLAN) spectrum. For fluorozirconate glass, C and $a\hbar\omega$ have been determined to be $1.59 \cdot 10^{10} \text{ s}^{-1}$ and 192.68 cm^{-1} , respectively [14]. In practical terms, the value of ΔE for each ion excited state determines if radiative decay will compete effectively with multiphonon emission. If ΔE for the state of interest exceeds a characteristic value for the host (and varies from host to host), then that state can be expected to be observed in emission. In fluorozirconate glass, for example, Reisfeld *et al.* [15] have noted that spontaneous emission has been observed from all Ho^{3+} excited states for which $\Delta E > 2100 \text{ cm}^{-1}$. In the case of the $^5\text{F}_5$ manifold, ΔE is $\sim 2200 \text{ cm}^{-1}$ and the highest phonon energy ($\hbar\omega$) for

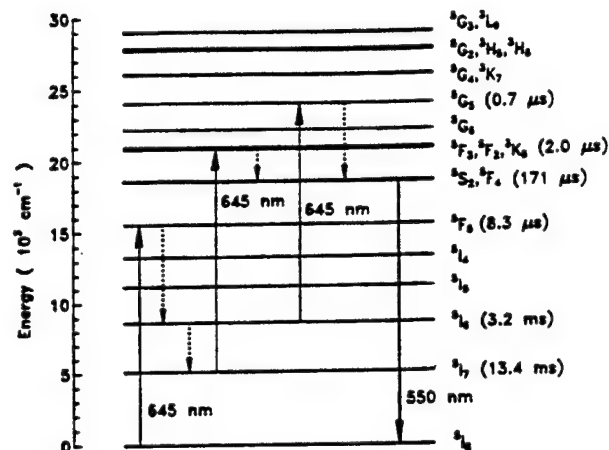


Fig. 1. Partial energy level diagram for Ho^{3+} showing the states and processes relevant to the $^5\text{S}_2 \rightarrow ^5\text{I}_8$ green upconversion laser. The absorption of a pump photon is represented by a thin solid line and the laser transition by the bold line. Dotted lines denote multiphonon emission and the lifetimes of several excited states [7], [10], [12], [13] are also indicated.

ZBLAN glass is $< 600 \text{ cm}^{-1}$ [12]–[15]. Consequently, the rate for deactivation of the $^5\text{F}_5$ state by multiphonon emission is $\sim 4 \cdot 10^5 \text{ s}^{-1}$ which gives rise to an overall $^5\text{F}_5$ lifetime of 8.3 μs . The lifetimes of both the $^5\text{I}_6$ and $^5\text{I}_7$ states, in contrast, are 3–13 milliseconds, making these levels well-suited as intermediate or “platform” states for the upconversion pumping process. The absorption of a second pump photon by the ion accesses (as indicated in Fig. 1) the $^5\text{G}_5$ or $^5\text{F}_3$ states which also relax nonradiatively to the comparatively long-lived $^5\text{S}_2$ level ($\tau \approx 171 \mu\text{s}$). Lasing occurs on the $^5\text{S}_2 \rightarrow ^5\text{I}_8$ transition of the ion which is calculated to have a stimulated emission cross-section at 300 K of $0.78 - 1.75 \cdot 10^{-20} \text{ cm}^2$ [15], [16]. Note that the overall quantum efficiency for this system is $2.25 \text{ eV}/(2 \cdot 1.92) \text{ eV} \approx 59\%$.

B. Ground State Depletion, Laser Spectra

Because the laser transition terminates on Stark sublevels of the ground state ($^5\text{I}_8$) of Ho^{3+} , depletion of the $^5\text{I}_8$ population has several significant implications for the performance of the green laser. One obvious area in which ground state depletion manifests itself is the absorption coefficient (α) at the pump wavelength, and Fig. 2 illustrates the results of measurements made at 643 nm for a fiber 21 cm in length. For $\geq 170 \text{ mW}$ of launched pump power, the absorption coefficient has declined from its peak (zero field) value by more than 30% and, at $P = 350 \text{ mW}$, $\alpha \approx 3.3\% \text{ cm}^{-1}$. The role of ground state absorption in the data of Fig. 2 is perhaps more clearly illustrated in Fig. 3 in which the pump power transmitted by the 21 cm fiber is plotted as a function of the launched pump power. For $\leq 150 \text{ mW}$ of launched power, the data display a quadratic dependence on pump power which is due to the combined effects of ground state and excited state ($^5\text{I}_6$, $^5\text{I}_7$) absorption. Above ≈ 180 – 200 mW of pump power, the $^5\text{F}_5 \leftarrow ^5\text{I}_8$ absorption process appears to have saturated (owing to the large oscillator strength for the transition) [13] and excited state absorption accounts for the linear behavior of the data. These conclusions are similar to those reached by Allain, Monerie, and Poignant in [7].

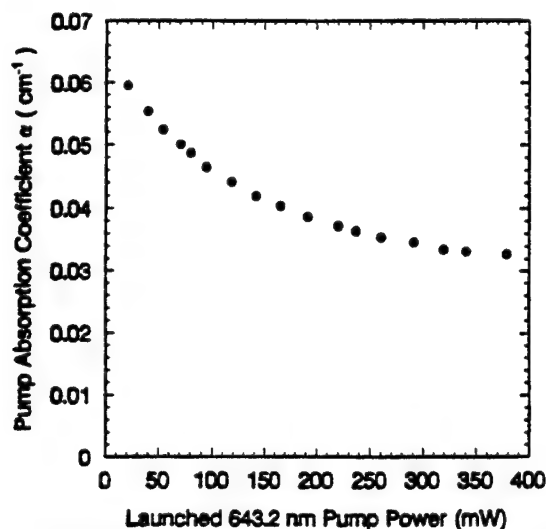


Fig. 2. Dependence of the absorption coefficient α on the pump power at 643 nm. These data were obtained for a fiber 21 cm in length.

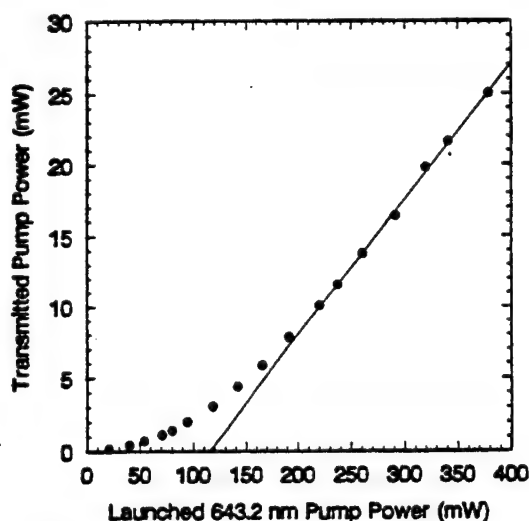


Fig. 3. Pump power at 643.2 nm transmitted by the 21 cm long fiber as a function of the launched power.

Extensive measurements of the $^5S_2 \rightarrow ^5I_8$ laser spectra were made at 77 K and room temperature for several values of pumping power, and the results also reflect the influence of ground state absorption. A low resolution spectrum of the fluorescence and laser emission at 300 K is given in Fig. 4 for a fiber 21 cm in length. Because of reabsorption by the ground (5I_8) state, the $^5S_2 \rightarrow ^5I_8$ spontaneous emission spectrum emerging from the fiber shifts progressively toward the red as the fiber is lengthened. For this length of fiber, the breadth of the spontaneous emission profile is >13 nm (FWHM) and, when a high- Q cavity is installed, lasing occurs on two dominant transitions that coincide with peak fluorescence. Spontaneous emission spectra recorded from the sidelight (i.e., 90° to the fiber) and fluorescence emerging from one end of a 21 cm long fiber are both shown in Fig. 4, and the effect of ground state absorption is evident.

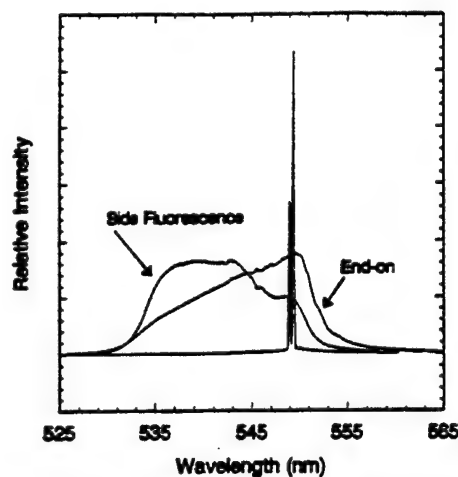


Fig. 4. Low resolution view of the fluorescence (both side and "end-on") and laser spectra for a ~ 21 cm long fiber pumped at 647.5 nm.

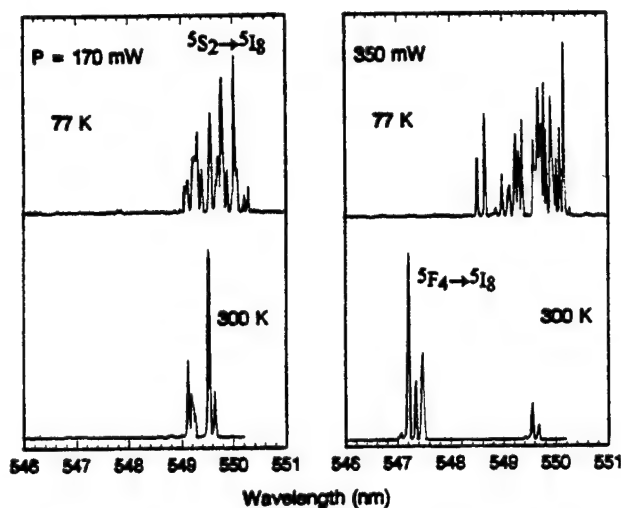


Fig. 5. Comparison of the laser spectra recorded for two values of pump power (incident on the pump optics) and operating temperature (77 and 300 K).

Some of the results recorded at various levels of pump power are summarized in Fig. 5 in which spectra produced by the untuned (free-running) laser when operating at 77 and 300 K and $P = 170$ and 350 mW are compared. All of the spectra were obtained from a fiber 19.5 cm in length. Although the spectra are congested and complex (partially due to the multiple sites occupied by the rare earth ion), several trends are clear. When the laser is operating at room temperature, increasing pump power results in the appearance and eventual dominance of lines at shorter wavelength. Specifically, at 300 K and $P = 170$ mW, the strongest laser lines are a pair lying between 549.1 and 549.6 nm. Increasing P beyond 250 mW leads to the appearance of several lines in the 547.2–547.6 nm interval and severe weakening of the longer wavelength transitions. The line at 547.2 nm is the most intense of those observed and, at still larger pump powers, this line remains dominant although new transitions at higher photon energies (547.05, 547.11 nm) are now present.

The emergence of the shorter wavelength features in the 300 K, 350 mW spectra is attributed to oscillation on the $^5F_4 \rightarrow ^5I_8$ transition of Ho^{3+} . Because the 5F_4 and 5S_2 states lie in close proximity to one another (energy separation of 114 cm^{-1} in Ho:YAG) [17], the two have, understandably, been treated as essentially one state in previous studies of lasing in the green from Ho^{3+} . In Fig. 5, note that the new lines emerge $\sim 74 \text{ cm}^{-1}$ to the "blue" of the now-weakened features grouped around 549.6 nm. Since this gap is consistent with the expected $^5S_2 - ^5F_4$ energy defect, the data suggest that: 1) the appearance of the short wavelength lines ($\lambda \sim 547 \text{ nm}$) cannot be attributed to the 5S_2 state, 2) because the 5F_4 and 5S_2 populations are presumably in thermal equilibrium, intense pumping increases the 5F_4 population above a threshold value, thus resulting in stimulated emission on the $^5F_4 \rightarrow ^5I_8$ transition, and 3) the stimulated emission cross-sections for the 547 nm ($^5F_4 \rightarrow ^5I_8$) transitions are greater than those for the 549 nm ($^5S_2 \rightarrow ^5I_8$) lines.

At 77 K, the behavior of the laser is markedly different, and the results point to the importance of the distribution of population among the Stark sublevels of the ground and 5S_2 states. All of the laser spectra acquired at this temperature consist of lines lying at $\lambda > 548.4 \text{ nm}$ but, as was the case for the room temperature data, the shortest wavelength lines (548.50, 548.65, 548.75 nm) are present only at the higher pump powers. These effects are attributed to partial depletion of several lower Stark sublevels of the ground state by the pump laser. For Ho^{3+} in LaF_3 , for example, the 5I_8 state has 17 Stark sublevels ($Z_1 - Z_{17}$) and at 300 K the Boltzmann factor for the highest-lying of these (at 409 cm^{-1}) is 14%. For level Z_7 , it has risen to $\sim 50\%$. Consequently, the thermal populations of even the most energetic 5I_8 sublevels are significant at 300 K which has an obvious impact on the threshold pumping power for a specific line. From the 77 K, $P = 350 \text{ mW}$ data, however, it appears that pumping the ion at $\sim 644 \text{ nm}$ suppresses the populations of several lower-lying 5I_8 Stark sublevels to such a degree that a population inversion with respect to the 5S_2 state is produced. Also, the appearance of lines in the 77 K laser spectra lying to the red of the room temperature lines is likely the result of thermal relaxation of both the 5S_2 and 5I_8 state populations. Before leaving this section, two other points should be made. One is that the depletion of ground state sublevels by the pump was discussed previously in connection with excitation spectra for the green laser [8]. Specifically, the excitation spectrum for the shortest wavelength laser lines ($\lambda \sim 547 \text{ nm}$) requires pumping wavelengths in a narrow region at the "blue" end of the $^5F_5 \leftarrow ^5I_8$ absorption spectrum and pump powers in excess of 300 mW. Also, we note that the power produced by the Ho:ZBLAN laser is considerably higher at 77 K than at room temperature, but all of the data to be presented later were acquired at 300 K.

C. Tuning Characteristics

With the two prism configuration described earlier, a 40 cm long fiber has been tuned over a $\sim 11 \text{ nm}$ region, and the results of several experiments are summarized in Fig. 6 for an

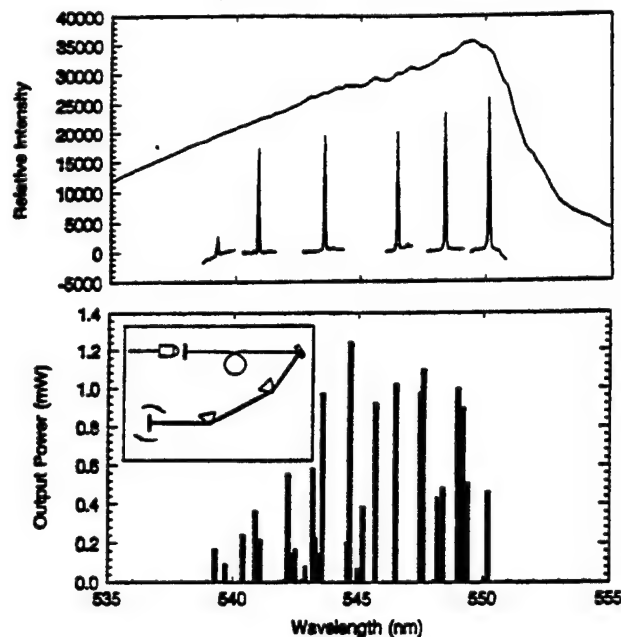


Fig. 6. Relative output power of the Ho:ZBLAN fiber laser at a variety of wavelengths in the green (~ 540 – 550 nm). Tuning was accomplished by installing two Brewster angle prisms inside the cavity, and all of the data were acquired with a $\sim 40 \text{ cm}$ long fiber and 430 mW of pump power at 645 nm. The upper half of the figure shows the spontaneous emission spectrum for the fiber and several laser spectra, representative of those observed as the laser was tuned. Only a few are shown for the sake of clarity. The lower portion of the figure illustrates the maximum output power that was obtained in the ~ 539 – 550 nm region for 1% of output coupling. The inset shows the experimental arrangement for the measurements. Although the threshold pump power for this arrangement was not measured precisely, it is estimated to be $\sim 250 \text{ mW}$.

incident pump power (at 645 nm) of 430 mW. The top portion of the figure shows the superposition of a number of spectra recorded over the full tuning range of the fiber. Note that lasing was obtained from ~ 539 – 550 nm with a single fiber. In [7], tunability over the 539–553 nm spectral interval was also demonstrated with $2.7 \mu\text{m}$ core diameter fibers. Although three fibers having lengths of 45, 103, and 121 cm were necessary to span the entire region, tuning from 541 to 553 nm was observed with the 121 cm long fiber.

Attempts to tune the laser continuously over this 10 nm region were unsuccessful owing to the inhomogeneously-broadened gain profile and, perhaps, the core diameter of the fiber and polarization effects, but, at most wavelengths at which oscillation occurred, single line operation (linewidth $< 0.1 \text{ nm}$) was obtained. The variation of the laser output power with wavelength is shown by the data in the lower portion of Fig. 6. Similar results for 20 and 80 cm fiber lasers are presented in Fig. 7.

D. Output Coupling Data

The dependence of laser output power on the absorbed pump power is illustrated in Fig. 8 for five values of cavity output coupling and a fiber 21 cm in length. Output couplings from 1–30% were studied in these experiments, and the largest output power obtained was 38 mW for 280 mW of absorbed pump power. Under these conditions, $\sim 35\%$ of the pump

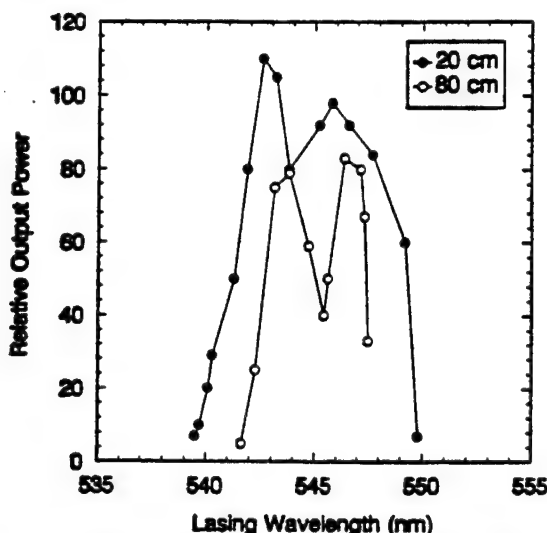


Fig. 7. Data similar to those of Fig. 6 illustrating the tuning characteristics of 20 and 80 cm fiber lasers.

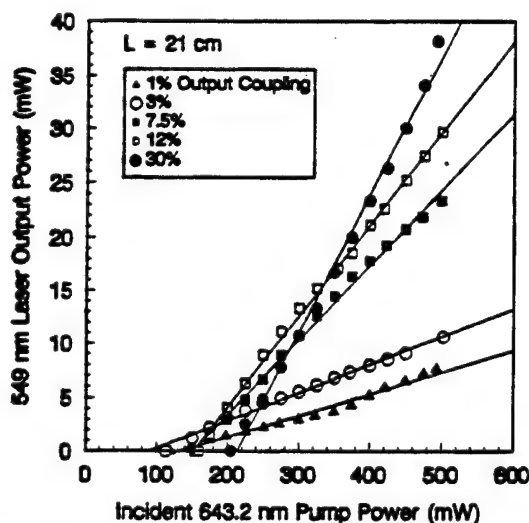


Fig. 8. Dependence of green output power on the incident pump power for a 21 cm long fiber and five values of cavity output coupling. Threshold pump powers (absorbed) varied between 66 and 130 mW, and the maximum slope efficiency and output power recorded were 24% and 38 mW, respectively. The solid lines represent linear, least-squares fits to the data.

power is not absorbed by the fiber. The threshold pump power ranged from 66–130 mW, and the maximum slope efficiency was 24%, which is to be compared to the value of 36% reported in [7] for a fiber ~ 45 cm in length and a core diameter of $2.7 \mu\text{m}$. Note that the output power shows no signs of saturating with respect to the output coupling or pump power. The solid lines in the figure represent the linear least-squares fit to each set of data.

Since all of the pump power is not absorbed by this short fiber, the green output power depends on the reflectivity of the cavity output coupler in the red as well as its transmission in the green. This was verified by using a second mirror (99% reflecting at 650 nm) behind the output coupler to redirect the transmitted pump beam back into the fiber. The result was increased output power, particularly for those output couplers

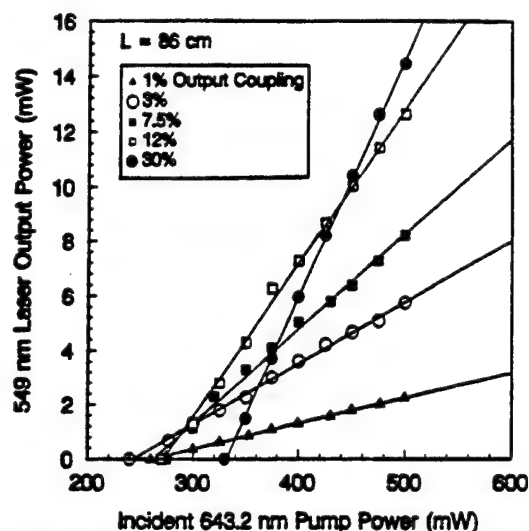


Fig. 9. Data similar to those of Fig. 8 for a fiber 86 cm in length. Threshold pumping powers (absorbed) ranging from 206–280 mW were measured (depending on the output coupling), and the largest output power obtained was 15 mW.

having low reflectivity at 650 nm. The data of Fig. 8 were obtained without the second mirror described above.

Similar data for an 86 cm long Ho:ZBLAN fiber are shown in Fig. 9. In this case, the maximum slope efficiency and output power recorded were 10% and 15 mW, respectively, and threshold pump powers ranged from 206 mW for 1% output coupling to 280 mW for 30% output coupling. Because of ground state absorption and the limited pump power available at present, the slope efficiency for the 86 cm fiber is considerably smaller than that for the shorter fiber. That is, absorptive losses from the weakly-pumped portion of the fiber limits the efficiency of the device and suggests that pumping from both ends of the fiber will be beneficial to overall performance. From the data of Figs. 8 and 9, one can readily extract the variation of the laser threshold pump power and slope efficiency with output coupling, and Fig. 10 illustrates the results. Although the threshold pump power increases linearly with output coupling (T), the slope efficiency appears to rise at a sublinear rate for $T > 10$ –15%, but more measurements at still higher values of output coupling will be necessary before firm conclusions can be reached.

E. Temporal Behavior of the Laser

For the pumping wavelength and power range of these experiments, the Ho:ZBLAN fiber laser operates in a quasi-CW mode. Specifically, it exhibits self-pulsing behavior, and Fig. 11 shows waveforms typical of those observed when the untuned laser is operating in the steady state. The top trace is a 50 ms segment of the waveform which consists of bursts of pulses having a duration of ~ 5 ms and occurring at a repetition frequency of ~ 100 Hz. An expanded view of a laser waveform is given in the lower portion of Fig. 11. The individual pulses ("spikes") within the bursts have temporal widths of $1 \mu\text{s}$ FWHM and recur at a rate of ~ 100 kHz. By varying the alignment of the input microscope objective with respect to

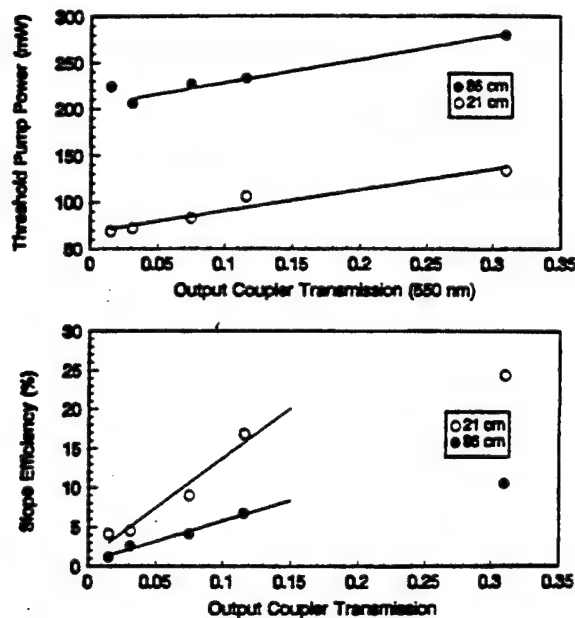


Fig. 10. Threshold pump power (top) and slope efficiency for the green Ho:ZBLAN laser as a function of the cavity output coupling (T). As denoted by the solid lines in the lower portion of the figure, the slope efficiency shows evidence of saturation for $T \geq 15\%$.

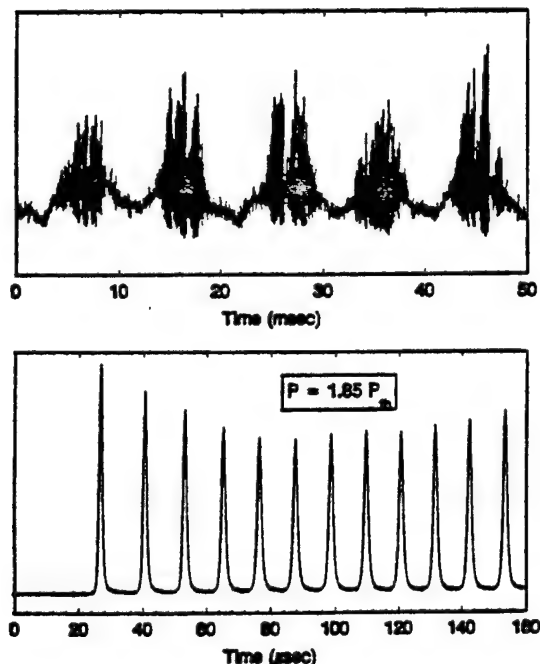


Fig. 11. Waveforms for the Ho:ZBLAN laser. (Top) 50 ms segment of the laser waveform for steady state conditions and a pumping power of $1.85 \times$ the threshold value (P_{th}). (Bottom) Expanded view of a segment of a typical laser waveform. The individual pulses have temporal widths (FWHM) of 1–2 μ s.

the fiber, it was possible to eliminate the bursts and obtain steady self-pulsing at the same frequency.

This behavior is similar to that reported for upconversion lasers in bulk crystals such as the Er^{3+} transition at 551 nm in fluoride crystals for which self-pulsing is now a familiar phenomenon [18]–[21]. Self-pulsing or “spiking” has previously

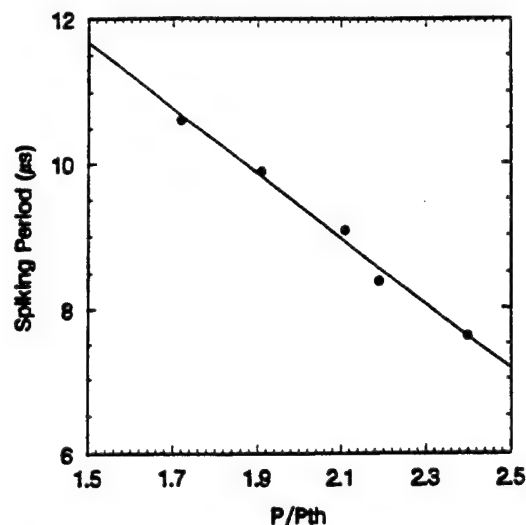


Fig. 12. Variation of the laser output spiking period with the pump power at 643 nm for a cavity output coupling of 1%. P_{th} is the threshold pumping power (120 mW incident on input coupling optics). The solid line represents the least-squares fit to the data.

been observed in erbium-doped infrared fiber lasers [22] and upconversion fiber lasers [1], [2] as well, and this phenomenon is common to solid-state lasers, in general. The periodicity of the oscillations, denoted τ , is a function of the pump power and data obtained for pump powers as large as $2.4 P_{th}$ (for 1% cavity output coupling) are shown in Fig. 12. Note that τ decreases linearly with increasing pump power and that the spiking period is roughly what one would expect for the buildup time for the $^5\text{S}_2$ population. Assuming: 1) the pumping intensity in the fiber core to be $\approx 10^5 \text{ W-cm}^{-2}$ and, 2) the time for the buildup of population in the upper laser level resulting from single photon transitions from the $^5\text{I}_6$ and $^5\text{I}_7$ states to be $\sim 10 \mu\text{s}$ ($P \sim 2 \cdot P_{th}$, Fig. 11), then the effective cross-section σ for the second stage of the pumping process is $\sim 3 \cdot 10^{-19} \text{ cm}^2$. In short, the dependence of τ on pump power is consistent with the expected pumping rate for the upper laser level. Consequently, we attribute the quasi-CW operation of the laser to self Q-switching which is a result of saturable loss in the active medium arising from ground state absorption. A magnified view of the early portion of the laser waveform observed when the pump beam is chopped (Fig. 13) shows the turn-on transient for the laser ($L = 22 \text{ cm}$) to be $\sim 300 \mu\text{s}$ (varies by $\pm 10\%$ from pulse-to-pulse).

IV. SUMMARY AND CONCLUSIONS

The output power and temporal and tuning behavior of the green ($\sim 549 \text{ nm}$) Ho:ZBLAN fiber laser has been studied for fibers ranging in length from ~ 20 to 86 cm. Output powers exceeding 38 mW have been measured for 280 mW of absorbed pump power and 30% cavity output coupling. For the highest output coupling studied to date (30%), the slope efficiency of the laser with respect to absorbed power is 24% for a multimode (11 μm core) fiber. Since the output power has not yet saturated with respect to either output coupling or pump power, it is likely that considerably higher output powers

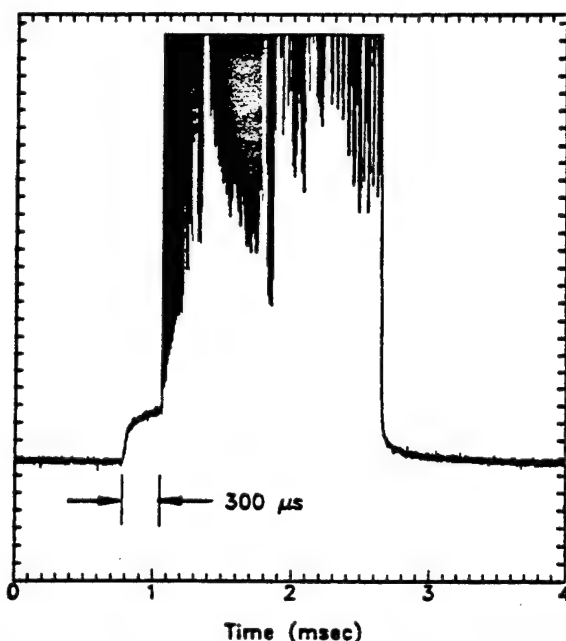


Fig. 13. Expanded view of the early portion of the Ho^{3+} laser waveform recorded when the pump beam is chopped.

and efficiencies will be realized with larger output couplings. Furthermore, the high NA (>0.3), single mode fibers that are currently available will undoubtedly yield considerably lower pump power thresholds than those reported here.

With two prisms installed in the optical cavity, the Ho fiber laser has been line-tuned over a ~ 11 nm region in the green. Although the laser currently operates in a self-pulsing mode, it appears that, in a manner similar to that observed for the $\text{Tm}:\text{ZBLAN}$ transition at 455 nm [23], the green $\text{Ho}:\text{ZBLAN}$ laser is capable of true CW operation with an alternate pumping scheme.

The role of the depletion of ground state population on laser performance is evident in the laser spectrum and conversion efficiency of the device. Because of ground state absorption losses, an ideal three-level laser is an inherently inefficient device. However, the behavior of the $\text{Ho}:\text{ZBLAN}$ fiber laser reported previously [2], [7], [8] as well as the results described earlier demonstrate that this laser is a quasi-3 level system in which strong depletion of the ground state can occur because of the presence of intermediate levels—namely, the $^5\text{I}_6$ and $^5\text{I}_7$ states of Ho^{3+} . Their ability to store energy drives the behavior of the $\text{Ho}:\text{ZBLAN}$ laser toward that of a four-level system.

Finally, by measuring the laser output power from the 21 cm long fiber as a function of cavity output coupling for the pump power fixed at 250 mW (threshold pump power for 20% output coupling), the small signal gain coefficient at 550 nm is estimated to be $0.9\% \cdot \text{cm}^{-1}$ for $P = 320$ mW. For the sake of comparison, it should be noted that the small signal gain coefficient for the blue-green (491 nm) and red (635 nm) lasing transitions in $\text{Pr}:\text{ZBLAN}$ fiber have been estimated by Tropper *et al.* [24] to be $\sim 0.2\% \cdot \text{cm}^{-1}$ and $2.7\% \cdot \text{cm}^{-1}$, respectively. The latter is the highest gain visible upconversion

laser demonstrated to date; in fact, the 635 nm line lases when the 4% reflection from one end of the cleaved fiber serves as the output coupler for the optical cavity. Consequently, the estimated small signal gain coefficient for $\text{Ho}:\text{ZBLAN}$ is intermediate to those for two well-known lasing transitions of the Pr^{3+} ion and is within a factor of three for the gain measured for the 635 nm line.

The slope efficiency and wide tunability of this fiber laser make it an attractive source for applications requiring green radiation, and the recent availability of red ($\lambda \sim 640$ nm) laser diodes suggests that a compact version of this fiber laser will be developed in the near future.

ACKNOWLEDGMENT

The authors gratefully acknowledge the technical assistance of J. L. Sexton and J. W. Carlson.

REFERENCES

- [1] J. Y. Allain, M. Monerie, and H. Poignant, "Blue upconversion fluorozirconate fiber laser," *Electron. Lett.*, vol. 26, pp. 166–168, 1990.
- [2] ———, "Room temperature CW tunable green upconversion holmium fiber laser," *Electron. Lett.*, vol. 24, pp. 261–263, 1990.
- [3] D. S. Funk, J. W. Carlson, and J. G. Eden, "Ultraviolet (381 nm), room temperature laser in neodymium-doped fluorozirconate fiber," *Electron. Lett.*, vol. 30, pp. 1859–1860, 1994.
- [4] ———, "Room temperature fluorozirconate glass fiber laser in the violet (412 nm)," *Opt. Lett.*, vol. 20, pp. 1474–1476, 1995.
- [5] D. S. Funk and J. G. Eden, "Glass fiber lasers in the ultraviolet and visible," *J. Select. Topics Quantum Electron.*, vol. 1, pp. 784–791, 1995.
- [6] S. G. Grubb, private communication.
- [7] J. Y. Allain, M. Monerie, and H. Poignant, "Characteristics and dynamics of a room temperature CW tunable green upconversion holmium fiber laser," in *Proc. 16th European Conf. Opt. Commun. (ECOC '90)*, 1990, vol. 1, pp. 575–578.
- [8] D. S. Funk, S. B. Stevens, and J. G. Eden, "Excitation spectra of the green $\text{Ho}:\text{fluorozirconate}$ glass fiber laser," *IEEE Photon. Technol. Lett.*, vol. 5, pp. 154–157, 1993.
- [9] Y. K. Voron'ko, A. A. Kaminskii, V. V. Osiko, and A. M. Prokhorov, "Stimulated emission of Ho^{3+} in CaF_2 at $\lambda = 5512 \text{ \AA}$," *Zh. Eksp. Teor. Fiz. Pis'ma Red.*, vol. 1, pp. 5–9, 1965; *JETP Lett.*, vol. 1, pp. 3–5, 1965.
- [10] L. F. Johnson and H. J. Guggenheim, "Infrared-pumped visible laser," *Appl. Phys. Lett.*, vol. 19, pp. 44–47, 1971.
- [11] D. S. Funk, S. B. Stevens, S. S. Wu, and J. G. Eden, "Characterization and modeling of the holmium upconversion fiber laser," in *Proc. SPIE*, 1994, vol. 2115, pp. 40–44.
- [12] M. D. Shinn, W. A. Sibley, M. G. Drexhage, and R. N. Brown, "Optical transitions of Er^{3+} ions in fluorozirconate glass," *Phys. Rev. B*, vol. 27, pp. 6635–6648, 1983.
- [13] K. Tanimura, M. D. Shinn, W. A. Sibley, M. G. Drexhage, and R. N. Brown, "Optical transitions of Ho^{3+} ions in fluorozirconate glass," *Phys. Rev. B*, vol. 30, pp. 2429–2437, 1984.
- [14] R. Reisfeld and C. K. Jørgensen, *Excited State Phenomena in Vitreous Materials*. Amsterdam, The Netherlands: Elsevier, 1987, pp. 1–90.
- [15] R. Reisfeld, M. Eyal, E. Greenberg, and C. K. Jørgensen, "Luminescence of six J-levels of holmium (III) in barium zirconium fluoride glass at room temperature," *Chem. Phys. Lett.*, vol. 118, pp. 25–28, 1985.
- [16] F. Gan and H. Zheng, "Spectral properties of Ho^{3+} ions in noncrystalline fluorides," *J. Non-Cryst. Solids*, vols. 95 and 96, pp. 771–776, 1987.
- [17] J. B. Gruber, M. E. Hills, M. D. Seltzer, S. B. Stevens, C. A. Morrison, G. A. Turner, and M. R. Kokta, "Energy levels and crystal quantum states of trivalent holmium in yttrium aluminum garnet," *J. Appl. Phys.*, vol. 69, pp. 8183–8204, 1991.
- [18] F. Tong, W. P. Risk, R. M. Macfarlane, and W. Lenth, "551 nm diode laser-pumped upconversion laser," *Electron. Lett.*, vol. 25, pp. 1389–1391, 1989.
- [19] R. A. McFarlane, "Dual wavelength visible upconversion laser," *Appl. Phys. Lett.*, vol. 54, pp. 2301–2302, 1989.
- [20] T. Herbert, W. P. Risk, R. M. Macfarlane, and W. Lenth, "Diode laser pumped 551 nm upconversion laser in $\text{YLiF}_4:\text{Er}^{3+}$," *Proc. Opt. Soc.*

Am. - Solid-State Lasers, H. P. Jenssen and G. Dubé, Eds., Washington, DC, Optical Society of America, 1990, vol. 6, pp. 379-383.

- [21] F. Heine, E. Heumann, T. Danger, T. Schweizer, G. Huber, and B. Chai, "Green upconversion continuous wave Er^{3+} : LiYF_4 laser at room temperature," *Appl. Phys. Lett.*, vol. 65, pp. 383-384, 1994.
- [22] F. Sanchez, P. LeBoudec, P.-L. François, and G. Stephan, "Effects of ion pairs on the dynamics of erbium-doped fiber lasers," *Phys. Rev. A*, vol. 48, pp. 2220-2229, 1993.
- [23] M. P. LeFlohic, J. Y. Allain, G. M. Stéphan, and G. Mazé, "Room temperature continuous wave upconversion laser at 455 nm in a Tm^{3+} fluorozirconate fiber," *Opt. Lett.*, vol. 19, pp. 1982-1984, 1994.
- [24] A. C. Tropper, J. N. Carter, R. D. T. Lauder, D. C. Hanna, S. T. Davey, and D. Szebesta, "Analysis of blue and red laser performance of the infrared-pumped praseodymium-doped fluoride fiber laser," *J. Opt. Soc. Am. B*, vol. 11, pp. 886-893, 1994.



David S. Funk received the B.S. degree in physics from the University of Puget Sound, Tacoma, WA, in 1989.

He is currently a graduate student in the Department of Physics at the University of Illinois, Urbana. His research interests include the study of rare earth-doped optical fiber and waveguide devices, and nonlinear optical waveguides.

S. B. Stevens, photograph and biography not available at the time of publication.

S. S. Wu, photograph and biography not available at the time of publication.



J. Gary Eden (S'75-M'76-SM'82-F'88) received the B.S. degree in electrical engineering from the University of Maryland, College Park, and the M.S. and Ph.D. degrees from the University of Illinois in 1973, and 1976, respectively.

He was awarded a National Research Council Postdoctoral Research Associateship from the Naval Research Laboratory, Washington, DC, in 1975. Subsequently, he joined the staff of the Laser Physics Branch of the NRL and, during his tenure there, made several contributions to the

areas of visible and ultraviolet lasers and gas laser spectroscopy, including co-discovery of the KrCl laser (222 nm) and the optically pumped HgCl and XeF lasers. Since 1979, he has been a member of the faculty of the Department of Electrical and Computer Engineering at the University of Illinois, Urbana. He is also a member of the graduate faculty in physics and currently serves as Associate Dean of the graduate college. His research group has demonstrated several new molecular lasers and amplifiers in the visible and near-IR (including CdI , ZnI and I_2 (500 nm)) and developed laser spectroscopic techniques for studying the Rydberg and autoionizing states of diatomic and triatomic molecules. Results in the latter area include rotationally resolving Rydberg-Rydberg transitions of the rare gas dimers (Ne_2 , Ar_2) and the spectroscopy of rare gas-halide molecules by photoassociation. He has also carried out extensive research on the growth of semiconductor and metal films by photochemical processes in the gas phase. His current research interests focus on upconversion lasers in waveguides and ultrafast, nonlinear techniques for generating coherent VUV radiation. He has published more than 130 papers, is the author of one book, and has been granted 12 patents.

Dr. Eden is Fellow of the IEEE, the American Physical Society, and the Optical Society of America. He recently served (1993-1995) as the Vice-President for Technical Affairs of the IEEE Lasers and Electro-Optics Society (LEOS) and is Editor of the LEOS book series *Progress in Lasers and Electro-Optics*.

Vibrational wave packets in the $C^1\Pi_u$ state of Cs_2 : Two color pump-probe experiments

G. Rodriguez,^{a)} P. C. John, and J. G. Eden

Everitt Laboratory, Department of Electrical and Computer Engineering, University of Illinois, Urbana, Illinois 61801

(Received 10 August 1995; accepted 11 September 1995)

Two color, pump-probe laser experiments on the ~ 100 fs time scale have been applied to examining the dynamics of vibrational wave packets in the $C^1\Pi_u$ state of Cs_2 . Wave packets consisting of more than 20 C state vibrational levels are produced with an initial pulse having a central wavelength between ~ 620 and 680 nm. The temporal history of the wave packet is inferred from the time and energy-integrated photoelectron signal produced when the excited state is photoionized by a time-delayed pulse centered at 605, 610, 615, 617, or 620 nm. Because of the difference in equilibrium internuclear separations for the $\text{Cs}_2(C)$ and $\text{Cs}_2^+(X)$ states ($\Delta R_e \sim 0.75$ Å), wave packets are readily observed (signal-to-noise ratio > 10) without the need to resort to mass selection techniques. Frequency analysis of the wave packet data shows a dominant (fundamental) component that decreases from 29 to ~ 28.3 cm^{-1} as the pump wavelength is tuned from 627 to 641 nm. Other spectral modes at ~ 23.5 and ~ 34 cm^{-1} and a weaker term at twice the fundamental frequency are also observed and quantum mechanical calculations of the wavepacket motion are in accord with the experimental results. © 1995 American Institute of Physics.

I. INTRODUCTION

Vibrational wave packets have proven to be an effective probe of interatomic potentials in diatomic molecules.¹⁻¹⁴ Since the motion of the wave packet is determined by the rovibrational levels from which it is composed and the electronic states with which it interacts, structural details regarding both dissociative and bound molecular states can be gleaned from analysis of the wave packet's temporal history. Previous experimental studies have demonstrated, for example, the utility of wave packets in observing the transition state associated with the photodissociation of diatomic and triatomic molecules such as NaI, ICN, and the thallium halides.^{4,5,8,15}

Wave packets produced in *bound* electronic excited states of small molecules oscillate between the classical inner and outer turning points of the potential with a periodicity determined primarily by the local energy spacing between vibrational states. Detecting the wave packets has been pursued along several avenues including: (1) monitoring fluorescence from the molecule itself or a dissociation product, and (2) photoionizing the excited state with a time-delayed (probe) pulse, followed by ion mass spectrometry and/or photoelectron spectroscopy. To date, studies of wave packets in bound excited states have been reported for only a few diatomic molecules, including I_2 , ICl , Na_2 , and Cs_2 (Refs. 7, 9, and 16-18).

The production and detection of wave packets in the bound $C^1\Pi_u$ state of Cs_2 with femtosecond laser pump-probe techniques were reported previously.¹⁸ In this paper, further two color experiments are described in which the wavelength of the probe pulse has also been varied. The wave packet is detected by photoionizing the excited dimer

with a time-delayed probe pulse and monitoring the resulting time and energy-integrated photoelectron current with a proportional counter (cylindrical diode). Frequency analysis of the wave packet data shows a dominant component that falls from 29 to ~ 28.3 cm^{-1} as the pump wavelength is tuned from 627 to 641 nm. Weaker modes are also observed at 23-24, 34-35, and ~ 58 cm^{-1} (i.e., the second harmonic of the fundamental mode). For pump wavelengths beyond ~ 645 nm, the frequency component at ~ 24 cm^{-1} intensifies and quantum mechanical calculations of the wave packet's motion in the $C^1\Pi_u$ state generally reproduce the experimental data.

II. EXCITED STATE STRUCTURE OF Cs_2

In the intervening six decades since the pioneering work of Loomis and Kusch,¹⁹ the structure of the ground and electronic excited states of the cesium dimer has been studied by a variety of spectroscopic techniques. Absorption spectroscopy has identified six major band systems in the visible and near infrared^{20,21} and the band peaking in the red ($\lambda \sim 625$ nm) is attributed to $C^1\Pi_u \leftarrow X^1\Sigma_g^+$ transitions of the dimer.²²⁻²⁵ Correlated with $\text{Cs}(5d^2D_{5/2}) + \text{Cs}(6s^2S_{1/2})$ in the separated atom limit,²⁶ the $C^1\Pi_u$ state of Cs_2 has a dissociation energy (D_e) determined from high resolution Fourier transform spectroscopy, Doppler-free polarization spectroscopy, and optical-optical double resonance spectroscopy by Amiot *et al.*²⁵ to be 2297.7 ± 0.8 cm^{-1} which is to be compared to the corresponding value for the ground state: $D_e(X^1\Sigma_g^+) = 3649.5 \pm 0.8$ cm^{-1} (Ref. 27). Furthermore, the $C^1\Pi_u$ potential is weakly predissociated by spin-orbit coupling with the $c^3\Sigma_u^+$ dissociative state^{28,29} which is derived from the $\text{Cs}(6p^2P_{3/2}) + \text{Cs}(6s^2S_{1/2})$ limit. In 1982, Raab *et al.*²⁴ suggested, on the basis of rotational line-width measurements, that the $c^3\Sigma_u^+$ potential intersects the $C^1\Pi_u$ state at $v > 10$ but subsequent laser excitation spec-

^{a)}Present address: CLS-5, MS-E543, Los Alamos National Laboratory, Los Alamos, NM 87545.

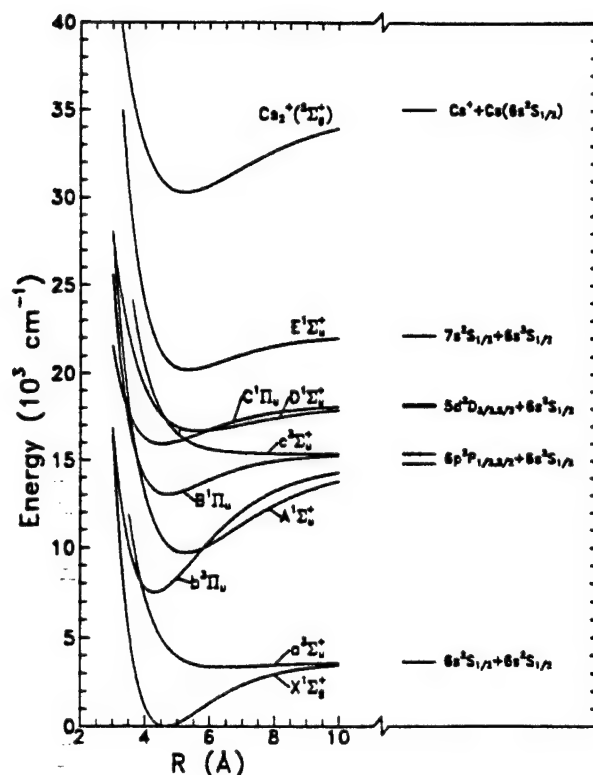


FIG. 1. Partial energy level diagram for Cs₂. All of the bound states are represented by Morse potentials for which the required spectroscopic constants are taken to be those of Table I. The potential shown for the dissociative $c^3\Sigma_g^+$ state is qualitative; its intersection with the $C^1\Pi_u$ potential reflects the conclusions reached in Ref. 24.

troscopic experiments conducted by Katô and co-workers^{30,31} indicate that the dissociative potential crosses the bound state between the classical inner turning points for $v'=0$ and 1. By measuring the dependence of the relative predissociation rate on v' , Baba *et al.*³¹ demonstrated that the rate peaks at $v'=3$ and that the data are best described by Mulliken's case c^- (Ref. 32)—that is, the repulsive state intersects the bound state at the latter's inner branch. For $v'=3$, the upper limit on the predissociation rate was estimated to be $3 \times 10^7 \text{ s}^{-1}$. Extensive studies of predissociation in the $D^1\Sigma_g^+$ state of Cs₂ have also been reported by the Kobe University group.^{33–35}

Figure 1 is a partial energy level diagram of Cs₂ that illustrates several of the excited states of the dimer that are relevant to the work described here. For convenience, all of

the bound states are represented by Morse potentials and the spectroscopic constants for each of the states are summarized in Table I.

III. EXPERIMENTAL APPARATUS AND DATA ACQUISITION

The approach adopted for these experiments is similar to that for previous studies of wave packet motion in bound states of diatomic molecules. An initial optical pulse having a duration (100–150 fs) less than the $C^1\Pi_u$ vibrational period (τ_v) produces a wave packet in the C state of the dimer by pumping the $C \leftarrow X$ transition. Since the $C^1\Pi_u$ vibrational frequency is $\sim 30 \text{ cm}^{-1}$ (cf. Table I), the bandwidth of the pump pulse is sufficient to coherently excite at least ten C state vibrational levels. Once the wave packet is established, its motion can be monitored indirectly by photoionizing the C excited state with a second time-delayed (probe) pulse (cf. Fig. 2). Prior studies have relied on detecting specific ions or measuring photoelectron energies with time-of-flight spectroscopies but, recently, it was demonstrated¹⁸ that the temporal history of the wave packet can also be determined by recording the time and energy-integrated photoelectron current. Wave packet data acquired for a single probe wavelength (620 nm) were shown to be consistent with the known spectroscopic constants for the $C^1\Pi_u$ state. More extensive data are reported here. The production and detection of wave packets in the C state have been explored in two color experiments in which the wavelengths of both the pump and probe are varied. Specifically, data have been acquired for the $C^1\Pi_u$ state when the central wavelength for the pump is varied between ~ 620 and 680 nm and the probe wavelength is 605, 610, 615, 617, or 620 nm.

Figure 3 is a schematic diagram of the experimental apparatus. The pulse train from which the pump and probe pulses were derived was generated by a colliding pulse mode-locked (CPM) laser and four stage amplifier system. Capable of generating $\sim 60 \text{ fs}$ (sech²) pulses at a repetition frequency of 90 MHz, the CPM oscillator is of conventional design and is pumped by 5.0 W (all lines) from a small frame Ar⁺ laser. Because of the limited available power, the CPM operates most reliably when producing pulses in the 80–100 fs range. Single pulse energies are typically 0.15 nJ (corresponding to an average output power approaching 15 mW) and the oscillator operates at a nominal wavelength of 625 nm and has a bandwidth of 8–10 nm. The four stage amplifier chain is based on the design of Fork *et al.*³⁶ and consists

TABLE I. Spectroscopic constants for several electronic states of Cs₂.

State	T_e (cm ⁻¹)	D_e (cm ⁻¹)	ω_e (cm ⁻¹)	$\omega_e x_e$ (cm ⁻¹)	B_e (cm ⁻¹)	R_e (Å)	Ref.
$X^1\Sigma_g^+$	0	3649.5	42.02	0.0819	0.011 74	4.648	27
$a^3\Sigma_g^+$	3360	290	11			6.4	27
$b^3\Pi_u$	7850	7300	50			4.3	20
$A^1\Sigma_g^+$	9450	5100	34			5.25	20
$B^1\Pi_u$	13 043.9	2139	34.33	0.0800	0.010 70	4.868	23
$C^1\Pi_u$	15 948.6	2297.7	29.66	0.0420	0.012 36	4.530	22,24,25
$D^1\Sigma_g^+$	16 699.8	1546	19.28	0.070	0.007 87	5.677	25,32
$E^1\Sigma_g^+$	20195	1989.7	28.99	0.1081	0.008 90	5.338	25

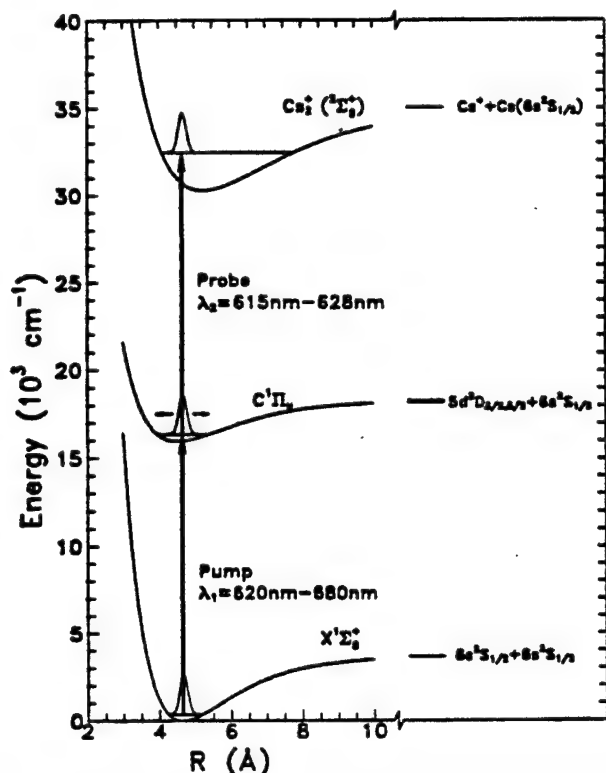


FIG. 2. Simplified potential energy level diagram for the cesium dimer illustrating the production of a wave packet in the $C' \Pi_u$ state and its subsequent detection by photoionization.

of longitudinally pumped stages driven by a frequency-doubled Nd:YAG laser [100 mJ, 2.5 ns full width at half maximum (FWHM), 30 Hz]. All of the amplifier cells contain kion red or sulforhodamine dye in water or methanol and the first three amplifiers are 2 cm path length cells pumped at 532 nm by 5, 9, and 17 mJ per pulse, respectively. The final amplifier is a quartz cell, ~7 cm in length, containing a solution of sulforhodamine dye in water and pumped by 50 mJ pulses from the Nd:YAG laser. Because the overall gain of the amplifier system is $\sim 3 \times 10^6$, it was necessary to suppress the generation of amplified spontaneous emission in the chain with a malachite green saturable absorber jet installed between the second and third amplifiers and a 75 μm diamond pinhole situated before the final amplifier. Group velocity dispersion introduced by the amplifiers broadens the pulse width to ~600 fs so a sequence of flint glass prisms was installed to recompress the pulses to below 80 fs. A representative intensity autocorrelation trace for the ~300 μJ pulses produced by this system is shown in Fig. 4.

Supercontinua generated by focusing the beam emerging from the amplifiers into a 1 cm path length cuvette containing water extend in wavelength from below 400 nm to >800 nm. After dividing the train of pulses into two, one is time delayed with respect to the other by a retroreflector mounted onto a computer-controlled micropositioner stage. The total available energy is divided roughly equally between the leading and trailing pulses and interference filters remove ~10 nm wide (FWHM) spectral segments from both pulses. Centered at wavelength λ_1 , the first set of broadband pulses serves as the pump for the Cs₂ C \leftarrow X transition. Rotating the filter is a convenient means for tuning λ_1 to the desired wavelength value and the pulse energies available in the con-

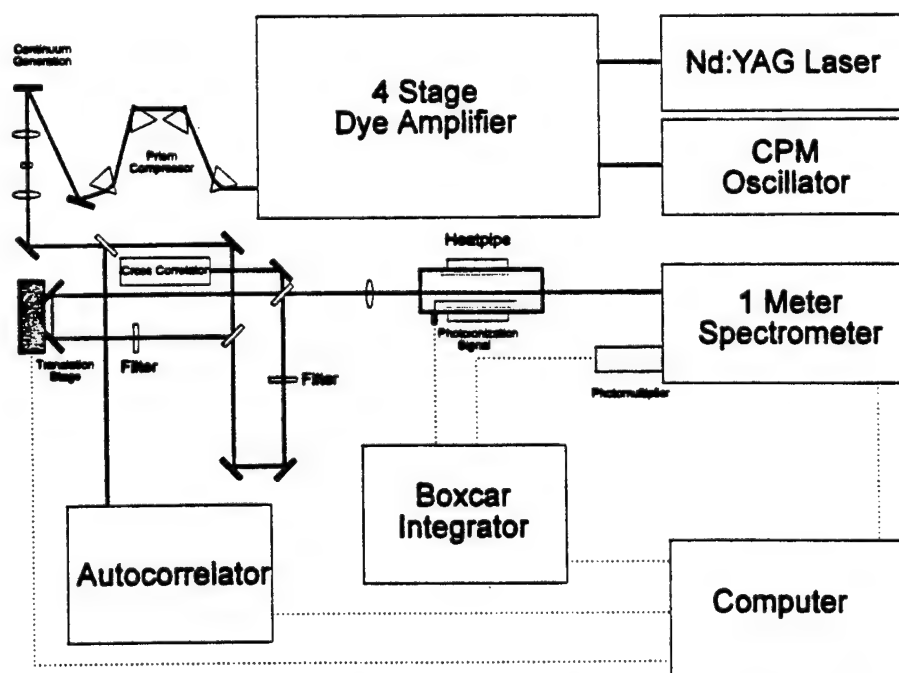


FIG. 3. Schematic diagram of the experimental apparatus, including the CPM oscillator, amplifier system and the data acquisition equipment. The overall gain of the amplifiers is $\sim 3 \times 10^6$, yielding single pulse energies of ~300 μJ . Two supercontinuum pulses are produced, one of which is time-delayed with respect to the other. Both trains of pulses (at a repetition frequency of 30 Hz) are directed into the heat pipe which contains a cylindrical diode.

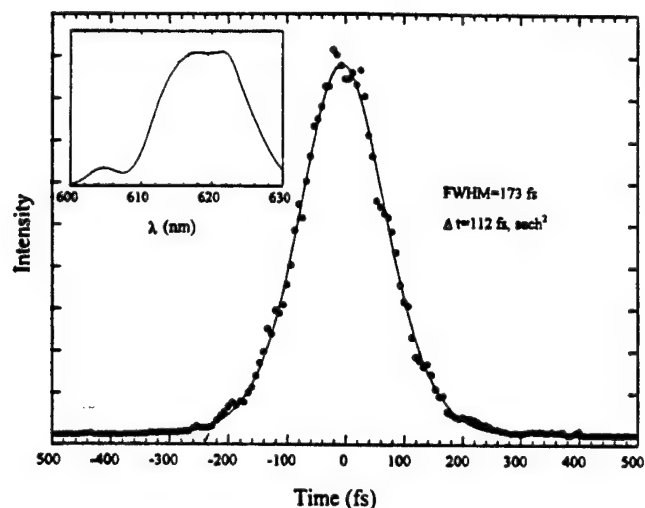


FIG. 4. Intensity autocorrelation trace that is representative of those obtained for the pulses produced by the CPM/amplifier system of Fig. 3. The inset illustrates the amplified pulse spectrum.

tinuum "slices" are typically several μJ . An intensity cross-correlation trace for a pulse associated with a $\lambda_1=642$ nm spectral segment is shown in Fig. 5. The dots in Fig. 5 are the cross-correlation data and the solid curve is the deconvolved profile for the pulse emerging from the interference filter, assuming that the pulses producing the supercontinuum have a sech^2 width of 110 fs (FWHM). Consequently, the temporal width of the continuum pulses is ~ 180 fs (sech^2).

The second (time-delayed) series of pulses serves as the probe of wave packet behavior by photoionizing the $C^1\Pi_u$ state. In a manner similar to that described for the pump pulses, continua centered at wavelength λ_2 and having a FWHM of ~ 10 nm are produced and directed colinearly with the pump pulses into a heat pipe containing Cs vapor. The time delay ($\equiv \Delta t$) between the pump and probe pulses

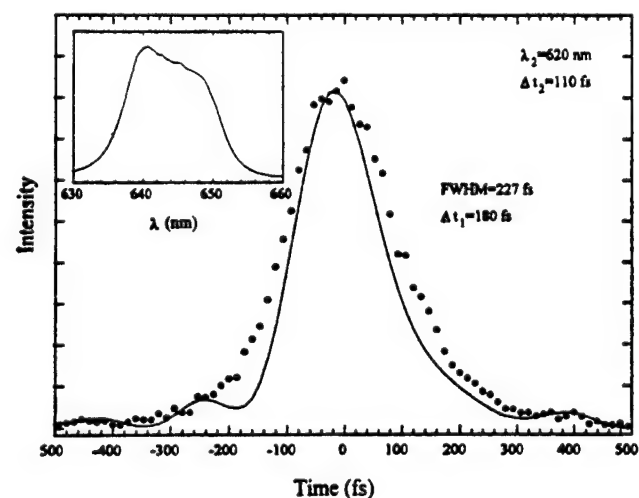


FIG. 5. Intensity cross correlation scan for a pulse associated with a supercontinuum segment centered at $\lambda_1=642$ nm. The dots represent the cross-correlation data (FWHM=227 fs) and the solid curve represents the deconvolved intensity profile for the tunable pulse, assuming a sech^2 pulse width of 110 fs for the 620 nm pump pulses producing the supercontinuum. The inset shows the corresponding spectrum for the $\lambda_1=642$ nm pulse.

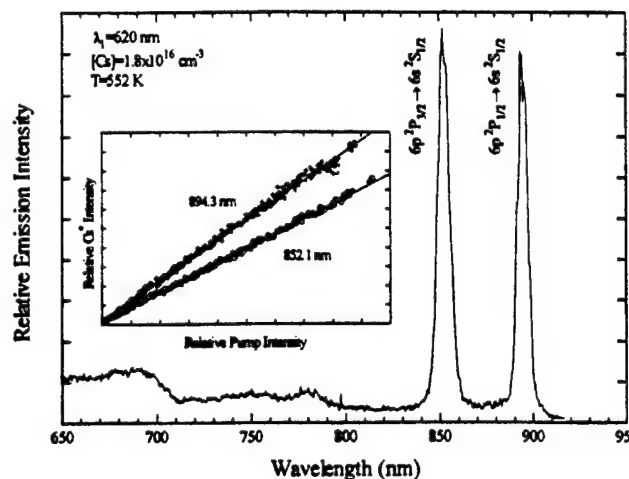


FIG. 6. Fluorescence spectrum observed when Cs vapor ($T=552$ K) is excited with $\lambda_1=620$ nm pulses. Both atomic and molecular emission is observed and the relative intensity of the Cs resonance lines at 852.1 and 894.3 nm scale linearly with the pump intensity (as shown by the inset). Weak emission at 690 and 780 nm is associated with the $B \rightarrow X$ and $D \rightarrow X$ transitions of Cs_2 , respectively. The atomic lines have intentionally been saturated.

can be adjusted in increments of 0.67 fs and, for the experiments described here, Δt was typically scanned between -2 and 20 ps. To summarize, both the pump and probe pulse wavelengths are discretely tunable. For the experiments described here, λ_1 was varied from ~ 620 to 680 nm and λ_2 was set to 605, 610, 615, 617, or 620 nm.

The heat pipe has a vapor zone 4 cm in length and contains a cylindrical diode (proportional counter) with which the time-integrated photoelectron current is monitored. After being evacuated to $<10^{-7}$ Torr, the heat pipe was loaded with 5 g of high purity (99.98%) Cs metal. Most of the data to be presented in the next section were obtained for a Cs vapor pressure of 10 Torr which corresponds to Cs and Cs_2 number densities of $1.5 \times 10^{17} \text{ cm}^{-3}$ and $2.4 \times 10^{15} \text{ cm}^{-3}$, respectively. The current pulse from the diode is preamplified and stored by a boxcar integrator which averages 300 shots for a given value of time delay between the pump and probe pulses.

IV. RESULTS AND DISCUSSION

A. Wave packet data: Temporal and frequency domains

As was discussed in Sec. II, it has long been known that spin-orbit coupling between the $C^1\Pi_u$ and $c^3\Sigma_u^+$ potentials induces weak predissociation of the C state and Fig. 6 illustrates the atomic and molecular fluorescence observed when Cs vapor is irradiated with single, ~ 100 fs pulses ($\lambda \approx 620$ nm). The inset to Fig. 6 shows the dependence of the Cs $6p^2P_{1/2,3/2} \rightarrow 6s^2S_{1/2}$ fluorescence intensity on the pump pulse intensity and confirms the presumption that only a single photon is required to access the C state.

Several sets of pump-probe experiments were conducted in which the pump wavelength λ_1 was varied over the ~ 620 –680 nm region while λ_2 was fixed at 605, 610, 615, 617, or 620 nm. Data representative of those obtained in

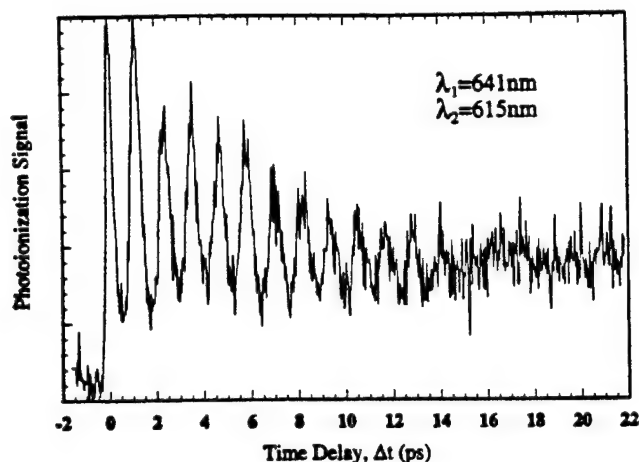


FIG. 7. Dependence of the photoelectron current (arbitrary units) on the time delay (Δt) between the pump and probe pulses (λ_1 and λ_2 , respectively). These data, acquired for $\lambda_1=641$ nm and $\lambda_2=615$ nm, are typical of those observed throughout the experiments. Note that no signal is observed for $\Delta t < 0$ (negative time delays as large as $\Delta t = -10$ ps were investigated). Other experimental parameters are: diode bias voltage (V)–150 V; $T=648$ K, $[\text{Cs}_2]=2.4 \times 10^{15} \text{ cm}^{-3}$.

these studies are shown in Fig. 7. The dependence of the time-integrated photocurrent on Δt is shown for $\lambda_1=641$ nm and $\lambda_2=615$ nm, where zero time delay was chosen to coincide with the maximum in the cross-correlation signal. The intense peak at $\Delta t=0$ presumably arises from two photon ionization of the dimer—a process that has been extensively studied in Cs₂ and is known to occur readily in the red.^{26,37} Multiphoton experiments reported by Suemitsu *et al.*³⁷ demonstrate that two photon ionization of Cs₂ in the 620–670 nm spectral region is resonantly enhanced by the $C^1\Pi_u$ state and, for single color (1+1 REMPI) experiments, the ion production rate peaks at ~ 627 nm.

The strong oscillations observed in the data of Fig. 7 for $\Delta t > 0$ (i.e., pump pulse precedes the probe) have a periodicity of 1.1–1.2 ps which is consistent with the expected classical vibrational period for the C state. Since the $C^1\Pi_u$ vibrational frequency ω_e is known to be 29.66 cm^{-1} (Ref. 25), then τ_e , the classical vibrational period, is $(c\omega_e)^{-1}=1.13$ ps. Note that the amplitude of the oscillations decreases rapidly and beyond ~ 15 ps no temporal variation of the photoionization signal is observable. Also, for negative time delays (probe precedes the pump), no signal was observed for $-10 \leq \Delta t \leq 0$ ps which is to be expected since the probe wavelength (615 nm) lies outside the $C \leftarrow X$ absorption band^{37,38} and, hence, a wave packet is not produced.

A summary of the scans in Δt acquired for five values of λ_1 (629–651 nm) but the probe wavelength λ_2 fixed at 615 or 617 nm is presented in Fig. 8. Similar data for λ_2 held constant at 605 nm are shown in Fig. 9 and scans obtained for $\lambda_2=620$ nm have been published previously.¹⁸ Considering all of the available data, several patterns are immediately evident. One noticeable trend is the gradual rise in the periodicity of the wave packet oscillations as the pump wavelength is increased which is a direct result of the changing composition of the wave packet for different pump wavelengths. Since this issue will be discussed in more detail in

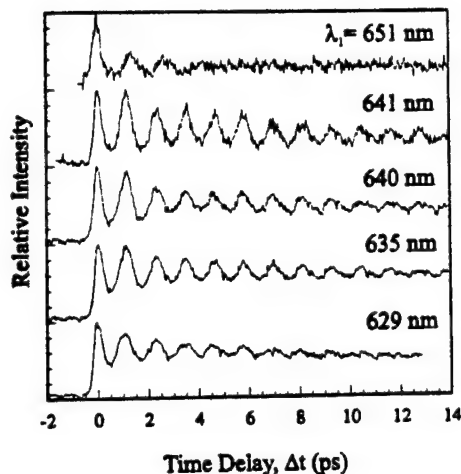


FIG. 8. Data similar to those of Fig. 7 for five different values of pump wavelength (λ_1) ranging from 629 to 651 nm but the probe wavelength (λ_2) fixed at 615 or 617 nm. For each of the scans, T was held constant at 648 K.

Sec. IV B, suffice it to say that tuning the pump wavelength to the red samples progressively *higher* C state vibrational levels (owing to the $C-X$ transition Franck–Condon factors); consequently, the vibrational energy declines and the vibrational period lengthens. Since the anharmonicity of the C state is weak ($\omega_e/\omega_e x_e \approx 700$), the variation of τ_e with λ_1 for most of the data of Figs. 8 and 9 is slight. Secondly, dephasing of the wave packet is not only evident from the decay of the amplitude of the oscillations but also their increasing temporal breadth. As λ_1 is increased, the wave packet dephases more quickly because the anharmonicity of the $C^1\Pi_u$ state introduces an additional phase factor into the expression for the wave function of the wave packet that is dependent upon the vibrational level, v' . For example, given a wave packet composed of the lowest 20 vibrational levels of the C state, the phase difference between the $v'=0$ and 20 components will be π at $t=20$ ps. Moreover, note that each of the photoionization current scans of Figs. 8 and 9 as well as Fig. 3 of Ref. 18 exhibit a component to the signal that is insensitive to Δt (or, expressed another way, the position of

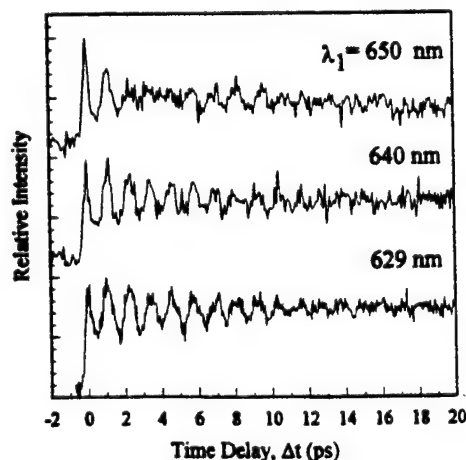


FIG. 9. Dependence of the photoelectron current on Δt for several pump wavelengths (629 to ~ 650 nm) and $\lambda_2=605$ nm; again, $T=648$ K.

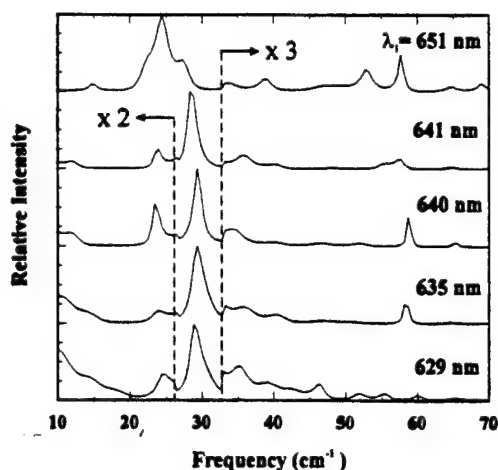


FIG. 10. Comparison of the frequency spectra for the data of Fig. 8 calculated by the maximum entropy method (MEM). Note the magnification of the spectrum for frequencies above $\sim 33 \text{ cm}^{-1}$ and below $\sim 27 \text{ cm}^{-1}$. For each value of λ_1 , three frequency components are noticeable; the dominant mode lies at $28\text{--}29 \text{ cm}^{-1}$ and two weaker components are reproducibly observed at $23\text{--}24 \text{ cm}^{-1}$ and $34\text{--}36 \text{ cm}^{-1}$. The number of poles in the computations was 200.

the wave packet), but the magnitude of this dc contribution is dependent upon the probe wavelength. In summary, it is reasonable to conclude that the data of Figs. 7–9 are consistent with the production and detection of vibrational wave packets in the $C^1\Pi_u$ state of Cs_2 .

As noted earlier, the periodicity of the oscillations observed in the scans of Figs. 8 and 9 change slowly with λ_1 for most of the pump wavelengths studied. In Fig. 8, for example, τ_c gradually rises from $\sim 1.15 \text{ ps}$ for $\lambda_1 = 629 \text{ nm}$ to $1.17\text{--}1.18 \text{ ps}$ for $\lambda_1 = 641 \text{ nm}$. The $\lambda_1 = 650$ and 651 nm data of Figs. 8 and 9, however, represent a distinct departure from the results obtained at shorter wavelengths. Not only is a change in periodicity observed ($\sim 1.4 \text{ ps}$), but the undulations in the $650\text{--}651 \text{ nm}$ traces vanish in ~ 3 vibrational periods ($< 4.5 \text{ ps}$). In contrast, oscillations in the $\lambda_1 = 629$, 635 , and $640\text{--}641 \text{ nm}$ data persist for $\Delta t > 8\text{--}9 \text{ ps}$.

Examination of the data of Figs. 7–9 in the frequency domain underscores these comments and yields several interesting results. Figure 10 compares the frequency spectra of the data acquired for $\lambda_1 = 629\text{--}651 \text{ nm}$ and $\lambda_2 = 615$ and 617 nm (Fig. 8). For the shorter pump wavelengths ($\lambda_1 = 629$, 635 , 640 , and 641 nm), the dominant frequency component peaks between 28 and 29 cm^{-1} , which is precisely what one would expect on the basis of the known vibrational constants for the C state. A slight shift of the fundamental mode to lower energies is observed as λ_1 is increased and the second harmonic is also consistently recorded in the $57\text{--}58 \text{ cm}^{-1}$ region. The third harmonic and other faint features in the frequency spectrum are difficult to detect reproducibly because the wavepacket signal persists for only ~ 10 vibrational periods. In Fig. 10 and those that follow, the frequency spectra were computed by the maximum entropy method (MEM). Gruebele and Zewail³⁹ have discussed the relative merits of the fast Fourier transform (FFT) and MEM in extracting the frequency components of the wave packet signal. Our experience is consistent with the guidelines suggested in

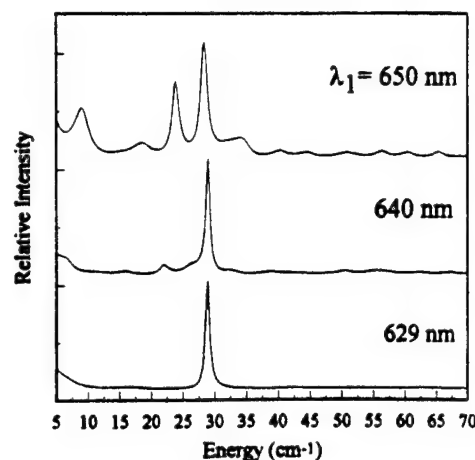


FIG. 11. Frequency (MEM) spectra for the (a) $\lambda_1 = 629 \text{ nm}$, and (b) $\lambda_1 \sim 650 \text{ nm}$ scans of Fig. 9 ($\lambda_2 = 605 \text{ nm}$). The traces shown were obtained for calculations in which the number of poles was taken to be 100.

Ref. 39—namely, the MEM approach provides more reliable peak positions than those resulting from analysis with an FFT, but it is essential that careful attention be paid to the number of poles in the calculation. Because of the limited lifetime of the wave packets studied here, it was not possible to implement the nonlinear fitting procedure described in Ref. 39.

An unexpected result is the presence of a third frequency mode lying at $\sim 24 \text{ cm}^{-1}$. Although weak in the $\lambda_1 = 629\text{--}641 \text{ nm}$ scans of Fig. 8, this peak is not an artifact of the data reduction process and intensifies dramatically in the $\lambda_1 = 650\text{--}651 \text{ nm}$ scans. The 28 cm^{-1} feature has diminished but is nevertheless still present. All of the data acquired to date yield the same result: namely, for pump wavelengths beyond $\sim 640 \text{ nm}$, the spectral feature at $\sim 24 \text{ cm}^{-1}$ grows in strength, regardless of the probe wavelength. Another weak frequency component is reproducibly observed in the $34\text{--}36 \text{ cm}^{-1}$ range. Similar results are obtained when the probe wavelength λ_2 is 605 or 620 nm and Fig. 11 presents representative data.

B. C-X Franck-Condon factors: Composition of the wave packet

Assuming the $C^1\Pi_u$ state potential to be adequately represented by the Morse function (for which the appropriate spectroscopic constants are given in Table I) and taking the $X^1\Sigma_g^+$ potential to be the IPA (inverted perturbation approach) curve of Raab *et al.*,²⁴ the Franck-Condon factors (FCF's) for the $C\text{--}X$ transition were calculated and their relative values (weighted by the ground state vibrational distribution) are illustrated graphically in Fig. 12. Because the equilibrium internuclear separations (R_e) for both states differ by $\sim 0.12 \text{ \AA}$, the (v', v'') transitions having the largest FCF's are those for which $v', v'' \leq 5$.

However, since the pump bandwidth ($\Delta \bar{\nu}_1$) is large compared to the vibrational frequency of the C state ($\sim 30 \text{ cm}^{-1}$) and more than 20 ground state vibrational levels of the dimer have significant thermal populations at the heat pipe operating temperature ($550\text{--}700 \text{ K}$), it is necessary to consider the

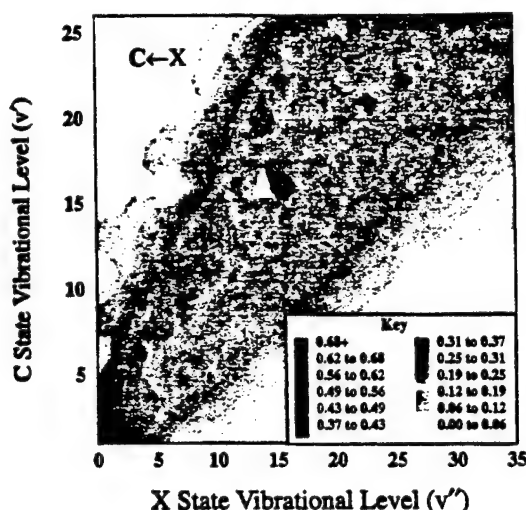


FIG. 12. Franck-Condon factors calculated for the $C \leftarrow X$ transition of Cs_2 and weighted by the relative populations of the X state vibrational levels at 600 K. In the computations it was assumed that the C state is adequately described by a Morse potential but the X state is described by the IPA potential of Ref. 24. The C state spectroscopic constants for the calculations are taken to be those listed in Table I.

contributions to formation of the wave packet from an unusually large number of $C^1\Pi_u$ vibrational levels. The distribution of population among the C state vibrational levels is described¹⁸ by the function

$$f(v') \propto \sum_{v''} P(v'', J'') \rho(v) |\langle \Psi_{v'} | \Psi_{v''} \rangle|^2, \quad (1)$$

where $\rho(v)$ is the laser spectral density factor at the frequency ν , $P(v'', J'')$ accounts for the ro-vibrational distribution in the thermalized ground state and the last term in Eq. (1) is the FCF for the $C \leftarrow X(v', v'')$ transition. The factor $P(v'', J'')$ is expressed as

$$P(v'', J'') = \frac{1}{Q_{\text{vib}} Q_{\text{rot}}} (2J'' + 1) \exp[-B_e'' J''(J'' + 1)/kT] \times \exp[-(E_{v''} - E_0)/kT], \quad (2)$$

where Q_{vib} and Q_{rot} are vibrational and rotational partition functions, respectively, for the $X^1\Sigma_g^+$ state, $E_{v''}$ is the vibrational energy of level v'' , and B_e is the first order rotational constant. In calculating $f(v')$, the $C-X$ transition moment was assumed to be independent of internuclear separation and the rotational temperature, T_r , was assumed to be the temperature of the vapor. For the sake of simplicity, only Q branch ($\Delta J=0$) rotational transitions ($J', J'' < 127$) were included in the calculations and $\rho(v)$ was taken to be a Gaussian function having a FWHM of $\Delta\nu_1$ (bandwidth of the pump pulse). For each value of pump wavelength, $f(v')$ was determined for the lowest 26 $C^1\Pi_u$ vibrational levels and the calculations encompassed all X state vibrational levels (v'') for which (v', v'') transitions had FCF's $\geq 10^{-3}$. The results are shown in Fig. 13 for $T=550$ K, $\lambda_1=627, 632, 637$ and 642 nm, and $0 \leq v' \leq 25$. One notices immediately that vibrational levels beyond $v'=15$ have appreciable popula-

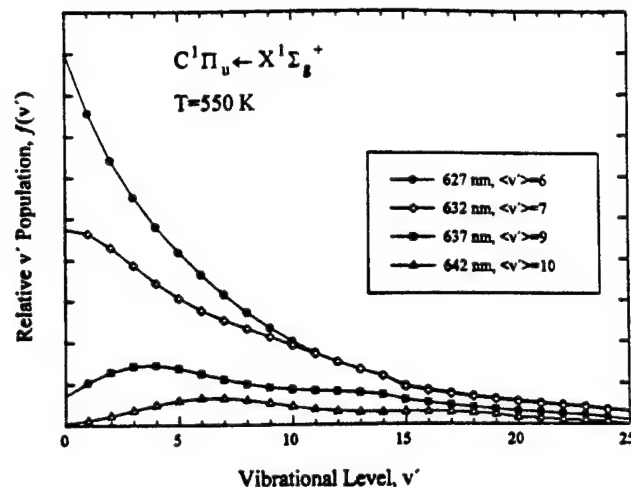


FIG. 13. Calculated $C^1\Pi_u$ vibrational population distribution function, $f(v')$, for pump wavelengths (λ_1) of 627, 632, 637, and 642 nm, assuming that the ground state ($X^1\Sigma_g^+$) vibrational manifold is thermalized at $T=550$ K. Also, the bandwidth of the pump is taken to be 10 nm (FWHM) and only Q branch rotational transitions and J'' values ≤ 127 have been considered. For each λ_1 , the mean excited state vibrational level ($\langle v' \rangle$) associated with $f(v')$ is indicated.

tions and that as λ_1 is increased from 627 to 642 nm, the distribution function steadily weakens and shifts to higher v' . As verified experimentally (cf. Fig. 8), the reduction in the area under $f(v')$ manifests itself in a diminished wave packet signal. This trend is perhaps best described by considering the mean vibrational level, $\langle v' \rangle$, for each of the distributions of Fig. 13. For example, the distribution function for $\lambda_1=627$ nm peaks at $v'=0$ but $\langle v' \rangle=6$ and the measured wave packet period more closely agrees with the value associated with $v'=6$ than that for $v'=0$. As will be discussed in Secs. IV C and IV D, the same conclusion holds for most of the data recorded in these experiments; namely, the temporal behavior of wave packets in the C state—particularly those composed primarily of $v' < 10$ vibrational states—is adequately described by the classical vibrational period for the mean level, $\langle v' \rangle$. From Fig. 13, it is also clear that, for each λ_1 , at least 20 vibrational states have populations no less than 10% of that for the most populated level. Consequently, the C state wave packets produced in these experiments are the coherent superposition of >20 vibrational wave functions which is 4–5 times larger than the set of eigenfunctions associated with previous studies of wave packet motion in bound states of diatomic molecules.^{11,17,40,41} In summary, as the pump is tuned deeper into the red, increasingly higher v' states contribute to the wave packet's composition and, in accord with experimental observations, the wave packet periodicity lengthens as the mean vibrational energy $(E_{\langle v' \rangle} - E_{\langle v' \rangle - 1})$ declines.

C. Wave packet simulations

1. Theory and numerical method

A quantum description of wave packet motion on a potential surface requires the computation of the time-dependent probability density for the state being probed. For the pump-probe experiments described earlier, the recorded

photoelectron signal, I_{sig} , is proportional to the wave packet probability density in the final state ($\text{Cs}_2^+(X^2\Sigma_g^+)$) in our case). That is:

$$I_{\text{sig}} \propto P(t) = \int_0^\infty \Psi^*(x, t) \Psi(x, t) dx \quad (3)$$

in which $\Psi(x, t)$, the nuclear wave function, can be calculated by second order, time-dependent perturbation theory. Two theoretical approaches for simulating the temporal history of the wave packet were compared in these studies but, in the discussion to follow, emphasis is placed on the density matrix approach described by Gruebele and Zewail.³⁹

In pump-probe experiments such as those reported here, the photoelectron current, measured as a function of time delay (Δt) between the pump and probe pulses, will reflect both vibrational and rotational coherences in the intermediate ($\text{Cs}_2 C^1\Pi_u$) state. For the limited range in Δt of interest here ($|\Delta t| \leq 22$ ps), however, the oscillatory behavior illustrated in Figs. 7–9 is predominantly associated with vibrational coherence and the dependence of the photoionization signal (I_{sig}) on Δt can be approximated by the expression:³⁹

$$I_{\text{sig}}(\Delta t) \propto \sum_i A_{i,i+1} (1 + b^2 \Delta t^2)^{-1} \times \{ \cos[2\pi c \Delta t (E_{i+1} - E_i) + \Delta \varphi_i] + b \Delta t \times \sin[2\pi c \Delta t (E_{i+1} - E_i) + \Delta \varphi_i] \}, \quad (4)$$

where E_i represents the energy of the i th vibrational level of $C^1\Pi_u$, $b = 2\pi\alpha_e k T_R (Bh)^{-1}$, B is an average rotational constant for the X state, T_R is the rotational temperature, $\Delta \varphi_i$ denotes a phase shift that, in general, will differ for each $C^1\Pi_u$ vibrational state contributing to the wave packet, and the summation is taken over all intermediate state vibrational levels that lie within the bandwidth of the pump. In considering the coherent transient represented by Eq. (4), several points should be made. Note first that only energy differences between adjacent vibrational levels are accounted for in this simplified relation but, in general, $E_{i+j} - E_i$ ($j > 1$) terms (i.e., $\Delta v \geq 2$) will also contribute and, as is evident in Fig. 9, are detectable in the Cs_2 wave packet's frequency spectrum. Moreover, although the rotational term does not sum over all J , it nevertheless introduces an effective phase and amplitude scaling factor that has the result of accelerating the dephasing of the wavepacket and, hence, the decay of the transient. The remaining experimental and molecular parameters, such as the pump laser spectrum, C - X FCF's and $X^1\Sigma_u^+$ population distribution, are represented by the A coefficients.

As noted earlier, a second set of simulations based on the theoretical approach described by Engel *et al.*^{42–44} were also carried out. Briefly, considering for the moment only the X and C states of Cs_2 , the wave function $\Psi_2(x, t)$ for the intermediate state (C state) wave packet produced by the pump pulse is given by first-order perturbation theory as

$$\Psi_2(x, t) = \frac{i}{\hbar} \int_{-\infty}^t U_2(t, t') \mu_{12} \cdot E_{12}(t') \Psi_1(x, t') dt', \quad (5)$$

where

$$\Psi_1(x, t') = \exp(-iE_1 t' / \hbar) \phi_1(x), \quad (6)$$

$$U_2(t, t') = \exp[-iH_2(t - t') / \hbar], \quad (7)$$

and $E_{12}(t)$ is the electric field vector for the pump radiation. In Eqs. (5) and (6), $\Psi_1(x, t)$ is the wave function of the initial state ($X^1\Sigma_g^+$), $\phi_1(x)$ is its corresponding time-independent radial wave function, and μ_{12} is the C - X electronic transition moment. A central role is played by the time propagator, $U_2(t + \delta t, t)$, which serves to advance the wave function(s) over small time intervals (t to $t + \delta t$) by introducing the incremental phase shift $\exp(-iH_2 \delta t / \hbar)$, where H_2 is the molecular Hamiltonian of the C state.

In a similar manner, the second step to these experiments—photoionization of the molecule—requires the inclusion of the Cs_2^+ ground state. From second-order perturbation theory, the wave function produced by the probe laser in the Cs_2^+ ground state is expressed as

$$\Psi_3(x, t) = \left(\frac{i}{\hbar} \right)^2 \int_{t_2}^t dt_2 \int_{-\infty}^{t_2} U_3(t, t_2) \mu_{23} \cdot E_{23}(t_2) U_2(t_2, t_1) \mu_{12} \cdot E_{12}(t_1) \Psi_1(x, t_1) dt_1 \quad (8)$$

in which the subscripts 1–3 refer, respectively to the $\text{Cs}_2 X$, C , and Cs_2^+ ground states. Equation (8) describes: (1) the promotion of the ground state wave function $\Psi_1(x, t_1)$ onto the intermediate state potential surface, $C^1\Pi_u$, with the pump optical field, $E_{12}(t_1)$, at time $t = t_1$; (2) the advancement of the intermediate state wavefunction in time with the propagator $U_2(t_2, t_1)$ until $t = t_2$, at which time the probe optical field, $E_{23}(t_2)$, “samples” the $C^1\Pi_u$ wave packet to form the Cs_2^+ wave function, $\Psi_3(x, t_2)$; and (3) the subsequent propagation of the final state wave function by $U_3(t, t_2)$ on the Cs_2^+ potential surface. Consequently, the final state wave function is calculated for each value of time delay ($\Delta t \equiv t_2 - t_1$) between the pump and probe lasers and the observed wave packet signal is then computed by invoking Eq. (3).

The FFT split operator or spectral method^{45,46} was used to solve for $\Psi_3(x, t)$ [Eq. (8)]. The split operator method relies on the speed of the FFT to transform the wave function between its coordinate and momentum representations in order to efficiently apply the time propagation operator, $U_2(t + \delta t, t)$, to the wave function. Doing so results in incremental phase shifts of the original wave function and the successive application of U q times propagates the wave function $q \cdot \delta t$ steps. The time propagation operator must be applied to the wavefunction at every coordinate grid point, x_n , at which the wave function is defined. A drawback of this method is that it is computationally intensive, requiring four FFTs for each time step of propagation. For all of the wave packet simulations presented here, the time step was typically chosen to be 2.5 fs and a coordinate grid length of 6 Å (3.5–9.5 Å) containing 512 grid points produced satisfactory (converging) results. Also, the initial state radial wave function, $\phi_1(x)$, is taken to be the X -state vibrational wave function, and the Hamiltonian operator assumes a Morse potential for the C state of Cs_2 for which the relevant spectroscopic constants are given in Table I. A Morse potential was also adopted for the ground state ($X^2\Sigma_g^+$) of Cs_2^+

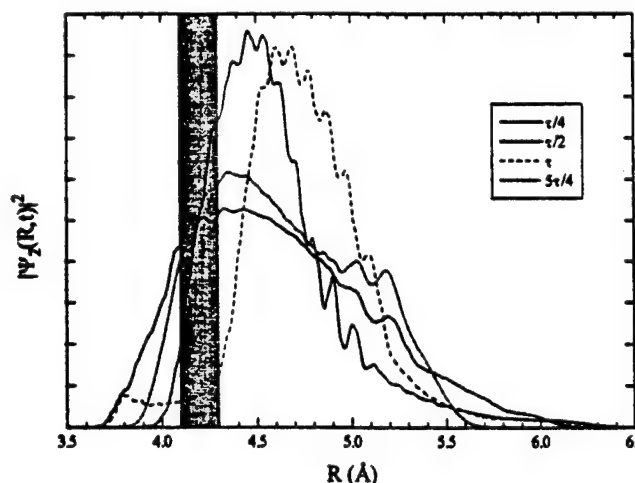


FIG. 14. Calculated wave packet probability density, $|\Psi_2(R,t)|^2$, for the $C\ ^1\Pi_u$ state for a pump wavelength of $\lambda_1=627$ nm. The first 26 vibrational levels of the ground state (thermalized at 550 K) are accounted for in the calculation. The vibrational period (τ_v) for the wave packet is 1.15 ps which is the same as that for the mean vibrational level, $\langle v' \rangle=6$. Several curves are shown which correspond to the probability density at various times following the generation of the wave packet. Also, the 4.1–4.3 Å region of internuclear separation is shaded because photoionization of the C state preferentially occurs in this interval (Ref. 18).

but most of its spectroscopic constants have yet to be measured. Several experimental values for the dissociation energy of the $X\ ^2\Sigma_g^+$ state have been published and Table I of Ref. 37 provides a recent summary of the available results. Only theoretical predictions exist for the equilibrium internuclear separation for $Cs_2^+(X)$ and the most recently published values^{47–49} lie between 5.20 and 5.25 Å. For the computational results that follow, the $Cs_2^+(X\ ^2\Sigma_g^+)$ constants were assumed to be $R_e=5.25$ Å, $D_e=5323\pm560$ cm⁻¹ (Ref. 49), $\omega_e=31$ cm⁻¹, and $\omega_e x_e=0.051$ cm⁻¹. The IPA potential for the Cs_2 ground state reported by Raab and co-workers²⁴ was again incorporated into the calculations. The electronic transition moment, μ_{ij} , for both the pump and probe transitions was assumed to be independent of internuclear separation, and the laser pulse width was typically set to be 150 fs for both the pump and probe pulses.

2. Numerical results

Figure 14 displays the calculated $C\ ^1\Pi_u$ state probability distribution, $|\Psi_2(R,t)|^2$, generated by pumping the $C\leftarrow X$ band with a 100 fs laser pulse at $\lambda_1=627$ nm. The calculation accounts for the thermal vibrational distribution in the ground state, and encompasses the first 26 vibrational levels of the $C\ ^1\Pi_u$ state. Four curves are shown in Fig. 14 to illustrate the probability distribution at several different times following the production of the wave packet. Note that the vibrational period for the wave packet (1.15 ps) is the same as that for the mean vibrational level, $\langle v' \rangle=6$. Over the course of a vibrational period, the spatial breadth of the wave packet expands and contracts as it oscillates about R_e for the C-state potential (4.53 Å).

A numerical simulation of the $\lambda_1=635$ nm, $\lambda_2=617$ nm photoionization current data of Fig. 8 is presented in Fig. 15 and compared with the experimental result. Also shown as

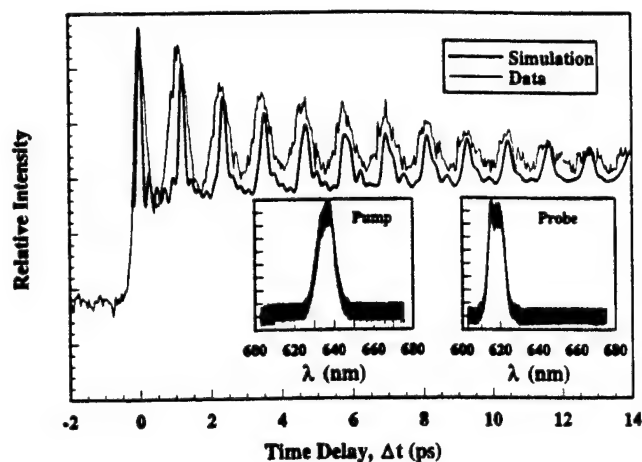


FIG. 15. Comparison of the numerical simulation (density matrix approach—Ref. 39) of the $\lambda_1=635$ nm, $\lambda_2=617$ nm scan of Fig. 8 with the experimental measurements. The two insets show the pump and probe spectra for the calculations.

insets to Fig. 15 are the measured pump and probe pulse spectra incorporated into the calculations. The experimental trace is reproduced reasonably well by the simulation, both in terms of the positions of the signal maxima and the decay of the amplitude peaks as the wave packet dephases. Similar results are obtained for other pump ($\lambda_1\leq 640$ nm) and probe wavelengths—namely, the experimental data are adequately described by the density matrix theoretical framework discussed earlier in this section.

A second example is given in Fig. 16 in which the photoionization data for $\lambda_1=651$ nm and $\lambda_2=615$ nm are compared to the simulation. Note that, again, most of the general features of the experimental trace and its corresponding frequency spectrum (shown by the inset) are present in the simulation. Both of the transients decay quickly (~ 5 ps) which reflects the rapid dephasing of the wave packet that is a result of the contribution of $v'>25$ states to the composi-

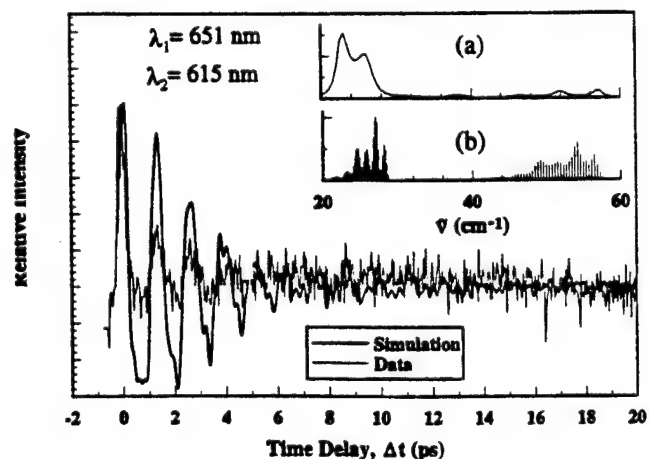


FIG. 16. Simulation of the wave packet temporal history for $\lambda_1=651$ nm and $\lambda_2=615$ nm compared with the experimental scan in Δt . The inset displays the corresponding (a) experimental and (b) calculated frequency spectra.

tion of the wave packet. For the $\lambda_1=629$ or 635 nm data of Fig. 8, for example, $v' > 25$ levels comprise a small portion of the wave packet but the reverse is true for λ_1 beyond ~ 645 nm. Since $\omega_e/\omega_e x_e$ for the C state is (as noted earlier) ~ 700 , then it is understandable that accelerated dephasing of the wave packet is observed when the anharmonic term in the series expansion for the $C^1\Pi_u$ vibrational energies [$G(v')$] is comparable to the harmonic term. In this instance, we expect this to occur for $v' \geq \sqrt{700} \approx 26$ which is consistent with the observations mentioned above. This trend is also clear in the frequency spectra. At low frequencies ($20\text{--}40\text{ cm}^{-1}$), the experimental spectrum peaks at ~ 24 and 26 cm^{-1} and is consistent with the MEM spectrum that has a maximum at 27 cm^{-1} but is skewed towards lower frequencies ($24\text{--}26\text{ cm}^{-1}$).

D. Discussion

In an earlier paper,¹⁸ it was shown that the ability to detect wave packets in the $C^1\Pi_u$ state and, more importantly, monitor their temporal behavior by measuring the relative photoelectron current is a consequence of the structure of the $\text{Cs}_2(C)$ and $\text{Cs}_2^+(X)$ states. In contrast to the C and X states of the neutral molecule, R_e for the $\text{Cs}_2(C)$ state differs from that of the ion by as much as 0.7 \AA . Consequently, photoionization of the $C^1\Pi_u$ state occurs predominantly in a narrow corridor at the classical inner turning points of high-lying ($v^+ \approx 65\text{--}90$) dimer ion vibrational states. That is, the photoionization signal of Figs. 7–9 oscillates with Δt because the FCFs for the $\text{Cs}_2^+(X) \leftarrow \text{Cs}_2(C)$ transition acquire most of their value at small R ($\approx 4.2\text{ \AA}$). An examination of $|\Psi_2(R, t)|^2$ in Fig. 14 reinforces this conclusion and qualitatively explains the success of measuring the total photoelectron yield—as the wave packet moves in the C state, the fraction of the probability density falling within the photoionization “window” ($\sim 0.2\text{ \AA}$ wide centered at $4.2\text{--}4.3\text{ \AA}$) (Ref. 18) oscillates and gradually diminishes as the wavepacket dephases. This work has expanded the results of Ref. 18 by demonstrating that probe wavelengths other than 620 nm are also suitable for detecting the wavepacket. Consequently, although the signal-to-noise ratio of the photoelectron signal declines rapidly for $\lambda_2 \leq 615\text{ nm}$, one can avoid the expense and complexity associated with time-of-flight ion or electron detection techniques.

One of the most intriguing aspects of the data of Figs. 7–11 is the results obtained for $\lambda_1 \geq 640\text{ nm}$. As was mentioned earlier, for example, the upper trace of Fig. 7 shows that the wave packet produced when $\lambda_1=651\text{ nm}$ dephases in ~ 3 vibrational periods, whereas the oscillations observed for shorter pump wavelengths persist for at least eight periods ($> 8\text{ ps}$). Corresponding changes in the MEM spectra are observed—the strongest frequency component in the $629 \leq \lambda_1 \leq 641\text{ nm}$ spectra is $28\text{--}29\text{ cm}^{-1}$ but, for $\lambda_1 \geq 645\text{ nm}$, declines to $\sim 23\text{--}24\text{ cm}^{-1}$.

As discussed earlier, these results are attributable to the rapidly changing composition of the wave packet as λ_1 is increased beyond $\sim 640\text{ nm}$. Although the anharmonic coefficient for the C state is modest ($\sim 0.04\text{ cm}^{-1}$), the distribution of population among the X state vibrational levels and

the $C\text{--}X$ FCFs result in wave packets composed predominantly of $v' \approx 10\text{--}40$ states. Consequently, at these pump wavelengths, the anharmonicity of the C state cannot be neglected, and the frequency spectrum of the wave packet noticeably shifts downwards.

In summary, two color pump–probe experiments have been described in which the dynamics of vibrational wave packets in the $C^1\Pi_u$ state of Cs_2 have been studied. Pump wavelengths between ~ 620 and 641 nm produce wave packets consisting of more than 20 vibrational wave functions—these wave packets dephase in $\sim 15\text{ ps}$ and exhibit oscillations that are in accord with the classical vibrational period. Frequency analysis of the wave packet's temporal history shows a fundamental frequency component that decreases from 29 to 28.3 cm^{-1} as the pump wavelength is tuned to the red. For pump wavelengths beyond $\sim 640\text{ nm}$, the anharmonicity of the $C^1\Pi_u$ state plays an increasingly important role as evidenced by a shift of the spectrum to frequencies below 28 cm^{-1} . Spectral modes at $23\text{--}24\text{ cm}^{-1}$ and at $34\text{--}36\text{ cm}^{-1}$ are also present and numerical simulations of the wave packet's motion are in accord with experimental results.

ACKNOWLEDGMENTS

Discussions with M. Gruebele and J. Lisy and the technical assistance of K. Voyles, J. Sexton, and K. Kuehl are gratefully acknowledged. This work was supported by the Air Force Office of Scientific Research and the National Science Foundation.

- ¹M. Dantus, M. J. Rosker, and A. H. Zewail, *J. Chem. Phys.* **87**, 2395 (1987).
- ²T. S. Rose, M. J. Rosker, and A. H. Zewail, *J. Chem. Phys.* **88**, 6672 (1988).
- ³M. J. Rosker, M. Dantus, and A. H. Zewail, *J. Chem. Phys.* **89**, 6113 (1988).
- ⁴T. S. Rose, M. J. Rosker, and A. H. Zewail, *J. Chem. Phys.* **91**, 7415 (1989).
- ⁵J. Misewich, J. H. Glowina, J. E. Rothenberg, and P. P. Sorokin, *Chem. Phys. Lett.* **150**, 374 (1988).
- ⁶M. Dantus, R. M. Bowman, M. Gruebele, and A. H. Zewail, *J. Chem. Phys.* **91**, 7437 (1989).
- ⁷R. M. Bowman, M. Dantus, and A. H. Zewail, *Chem. Phys. Lett.* **161**, 297 (1989).
- ⁸J. Misewich, J. H. Glowina, and P. P. Sorokin, *J. Chem. Phys.* **92**, 3335 (1990).
- ⁹M. Gruebele, G. Roberts, R. M. Bowman, and A. H. Zewail, *Chem. Phys. Lett.* **166**, 459 (1990).
- ¹⁰L. R. Khundkar and A. H. Zewail, *Ann. Rev. Phys. Chem.* **41**, 15 (1990).
- ¹¹T. Baumert, B. Bühler, R. Thalweiser, and G. Gerber, *Phys. Rev. Lett.* **64**, 733 (1990).
- ¹²M. Gruebele, G. Roberts, and A. H. Zewail, *Philos. Trans. R. Soc. London, Ser. A* **332**, 35 (1990).
- ¹³M. Dantus, M. H. M. Janssen, and A. H. Zewail, *Chem. Phys. Lett.* **181**, 281 (1991).
- ¹⁴M. Gruebele, I. R. Sims, E. D. Potter, and A. H. Zewail, *J. Chem. Phys.* **95**, 7763 (1991).
- ¹⁵M. Dantus, M. J. Rosker, and A. H. Zewail, *J. Chem. Phys.* **89**, 6128 (1988).
- ¹⁶M. H. M. Janssen, R. M. Bowman, and A. H. Zewail, *Chem. Phys. Lett.* **172**, 99 (1990).
- ¹⁷T. Baumert, M. Grosser, R. Thalweiser, and G. Gerber, *Phys. Rev. Lett.* **67**, 3753 (1991).
- ¹⁸G. Rodriguez and J. G. Eden, *Chem. Phys. Lett.* **205**, 371 (1993).
- ¹⁹F. W. Loomis and P. Kusch, *Phys. Rev.* **46**, 292 (1934).
- ²⁰R. P. Benedict, D. L. Drummond, and L. A. Schlie, *J. Chem. Phys.* **66**, 4600 (1977).

- ²¹R. Gupta, W. Happer, J. Wagner, and E. Wennmyr, *J. Chem. Phys.* **68**, 799 (1978).
- ²²P. Kusch and M. M. Hessel, *J. Mol. Spectrosc.* **25**, 205 (1968).
- ²³P. Kusch and M. M. Hessel, *J. Mol. Spectrosc.* **32**, 181 (1969).
- ²⁴M. Raab, G. Hönig, W. Demtröder, and C. R. Vidal, *J. Chem. Phys.* **76**, 4370 (1982).
- ²⁵C. Amiot, W. Demtröder, and C. R. Vidal, *J. Chem. Phys.* **88**, 5265 (1988).
- ²⁶C. B. Collins, F. W. Lee, J. A. Anderson, P. A. Vicharelli, D. Popescu, and I. Popescu, *J. Chem. Phys.* **74**, 1067 (1981).
- ²⁷H. Weickenmeier, U. Diemer, M. Wahl, M. Raab, W. Demtröder, and W. Müller, *J. Chem. Phys.* **82**, 5354 (1985).
- ²⁸This state is occasionally labeled $b^3\Sigma_u^+$ or $(2)^3\Sigma_u^+$ in the literature.
- ²⁹E. K. Kraulinya, S. M. Papernov, and M. L. Janson, *Chem. Phys. Lett.* **63**, 531 (1979).
- ³⁰H. Katô, K. Yokoyama, M. Baba, N. Tamai, I. Yamazaki, and S. Nagakura, *J. Chem. Phys.* **87**, 1987 (1987).
- ³¹M. Baba, T. Nakahori, T. Iida, and H. Katô, *J. Chem. Phys.* **93**, 4637 (1990).
- ³²R. S. Mulliken, *J. Chem. Phys.* **33**, 247 (1960).
- ³³K. Yokoyama, M. Baba, and H. Katô, *J. Chem. Phys.* **89**, 1209 (1988).
- ³⁴H. Katô, T. Kobayashi, M. Chosa, T. Nakahori, T. Iida, S. Kasahara, and M. Baba, *J. Chem. Phys.* **94**, 2600 (1991).
- ³⁵T. Kobayashi, T. Usui, T. Kamauchi, M. Baba, K. Ishikawa, and H. Katô, *J. Chem. Phys.* **98**, 2670 (1993).
- ³⁶R. L. Fork, C. V. Shank, and R. T. Yen, *Appl. Phys. Lett.* **41**, 223 (1982).
- ³⁷H. Suemitsu, H. Kitaura, and K. Seki, *J. Phys. Soc. Jpn.* **62**, 3425 (1993), and references cited therein.
- ³⁸M. Lapp and L. P. Harris, *J. Quant. Spectrosc. Radiat. Trans.* **6**, 169 (1966).
- ³⁹M. Gruebele and A. H. Zewail, *J. Chem. Phys.* **98**, 883 (1993).
- ⁴⁰T. Baumert, B. Bühler, M. Grosser, R. Thalweiser, V. Weiss, E. Wiedenmann, and G. Gerber, *J. Phys. Chem.* **95**, 8103 (1991).
- ⁴¹T. Baumert, V. Engel, C. Röttgermann, W. T. Strunz, and G. Gerber, *Chem. Phys. Lett.* **191**, 639 (1992).
- ⁴²V. Engel, H. Metiu, R. Almeida, R. A. Marcus, and A. H. Zewail, *Chem. Phys. Lett.* **152**, 1 (1988).
- ⁴³V. Engel and H. Metiu, *J. Chem. Phys.* **90**, 6116 (1989); **91**, 1596 (1989).
- ⁴⁴H. Metiu and V. Engel, *J. Chem. Phys.* **93**, 5693 (1990).
- ⁴⁵M. D. Feit and J. A. Fleck, *J. Chem. Phys.* **78**, 301 (1983).
- ⁴⁶M. D. Feit and J. A. Fleck, *J. Chem. Phys.* **80**, 2078 (1984).
- ⁴⁷L. Von Szentpaly, P. Fuentealba, H. Preuss, and H. Stoll, *Chem. Phys. Lett.* **93**, 555 (1982).
- ⁴⁸M. Krauss and W. J. Stevens, *J. Chem. Phys.* **93**, 4236 (1990).
- ⁴⁹A. Wetmore, F. K. Men, M. Kimura, and R. E. Olson (unpublished).

Room-temperature fluorozirconate glass fiber laser in the violet (412 nm)

D. S. Funk, J. W. Carlson, and J. G. Eden

Everitt Laboratory, Department of Electrical and Computer Engineering, University of Illinois, Urbana, Illinois 61801

Received February 24, 1995

Continuous oscillation on the $^2P_{3/2} \rightarrow ^4I_{11/2}$ transition of Nd^{3+} in a fluorozirconate glass (ZBLAN) fiber at room temperature has been observed. When pumped at ~ 590 nm, a Nd:ZBLAN fiber 39 cm in length lases in the violet at 412 nm and produces ~ 0.5 mW of power for 320 mW of pump power and a cavity output coupling of 0.4%. The breadth of the laser's excitation spectrum is ~ 12 nm (581–593 nm).

Upconversion fiber lasers offer an efficient approach to converting red or near-infrared photons into coherent visible or ultraviolet radiation. The fabrication and availability of rare-earth-doped fluorozirconate glass (ZBLAN) fiber has proven to be the key development in realizing visible fiber lasers because the characteristics of ZBLAN glass, combined with the inherent advantages of the fiber geometry, are responsible for the performance of these devices. Because of a phonon spectrum confined to low energies ($< 3kT$, $T = 300$ K), the telluride or heavy-metal fluoride glasses such as ZBLAN minimize deactivation of rare-earth-excited states by multiphonon processes, thereby lengthening the effective lifetimes of ion excited states that are pivotal to the upconversion process.¹ In conjunction with the extended pump/gain medium interaction lengths afforded by fibers, this property of ZBLAN underlies the success in demonstrating a variety of cw, rare-earth-doped fiber lasers over the past five years.^{2–6} The fiber geometry is particularly beneficial when the pump absorption is weak or the stimulated emission cross section is small, and, in numerous cases, transitions that have been demonstrated to lase at room temperature in ZBLAN fibers have required cooling for lasing to occur in a bulk fluoride crystal. Furthermore, the fiber length permits small rare-earth concentrations to be used in cases in which ion-ion interactions are detrimental to the overall efficiency of the system.

Wavelengths throughout the near-infrared and visible are now available from compact fiber lasers operating at room temperature, and recently what is to our knowledge the first ultraviolet fiber laser, based on Nd-doped ZBLAN fiber, was reported.⁷ This Letter describes the demonstration of lasing on the $^2P_{3/2} \rightarrow ^4I_{11/2}$ transition of Nd^{3+} at 412 nm in a ZBLAN fiber. At room temperature the device operates cw and ~ 0.5 mW of output power is obtained for $\sim 0.4\%$ output coupling. In 1989, Tong *et al.*⁸ reported lasing at 413 nm from a Nd:YLiF₄ crystal cooled to below 40 K.

The active medium for these experiments is a Nd-doped ZBLAN fiber having a core diameter of $2.2 \mu\text{m}$, a NA of 0.15, and a Nd concentration in the core of 1000 ppm (by weight). Consequently the cutoff wavelength is 400 nm. Two mirrors butted directly against the polished ends of the fiber formed

the optical cavity. One of the mirrors is a dichroic through which the pump is launched into the fiber. It is flat and transmits $\sim 0.3\%$ at 412 nm and $> 95\%$ at 590 nm. When a $10\times$ microscope objective is used to couple the pump beam from an Ar-ion-pumped ring dye laser into the fiber, the launching efficiency is estimated to be 30%. The second mirror has a radius of curvature of 10 cm and a transmission of 0.1% at 412 nm. Therefore, the overall output coupling of the cavity is 0.4% and the power measurements reported here represent the sum of the outputs measured from both ends of the fiber.

A $5\times$ microscope objective collimated the radiation emerging from the 0.1%-transmitting mirror, and spectra were recorded with a diode array coupled to a 0.25-m spectrograph having a reciprocal dispersion (in first order) of 6 nm/mm. Power measurements were made with a calibrated calorimeter, and the transient behavior of the laser was examined with a 500-MHz-bandwidth oscilloscope and a photomultiplier. All experiments were carried out at room temperature.

Figure 1 shows the spontaneous emission and laser spectra in the ~ 360 – 430 -nm region for a Nd:ZBLAN fiber pumped at 590 nm. As reported previously,⁷ two intense fluorescence peaks, centered at 381 and 412 nm, are observed and are attributed to $^4D_{3/2} \rightarrow ^4I_{11/2}$ and $^2P_{3/2} \rightarrow ^4I_{11/2}$ transitions of the Nd^{3+} ion, respectively.^{8,9} Once the optical cavity is installed, lasing occurs at 412 nm and the measured spectral linewidth of the violet beam is < 0.1 nm. As depicted in Fig. 2, the absorption of a 590-nm photon excites the $^4G_{5/2}$ state, which subsequently relaxes by multiphonon emission to populate the $^4F_{3/2}$ manifold. Upon absorbing a second pump photon, the ion is excited to states lying immediately above the $^4D_{3/2}$ level, which also relax nonradiatively to the $^4D_{3/2}$ and $^2P_{3/2}$ states. Joubert *et al.*⁹ measured the spontaneous emission lifetimes for the $^4F_{3/2}$ "platform" state and the $^2P_{3/2}$ upper laser level to be 470 and 50 μs , respectively, in Nd:BaY₂F₈.

Measurements of the dependence of the 412-nm output power on the pump power (at 590 nm) are summarized in Fig. 3 for a fiber 39 cm in length. The onset of oscillation is observed when the pump power incident on the input optics is ~ 225 mW. Output powers approaching 0.5 mW have been recorded for a pump power of 320 mW. For pump powers beyond

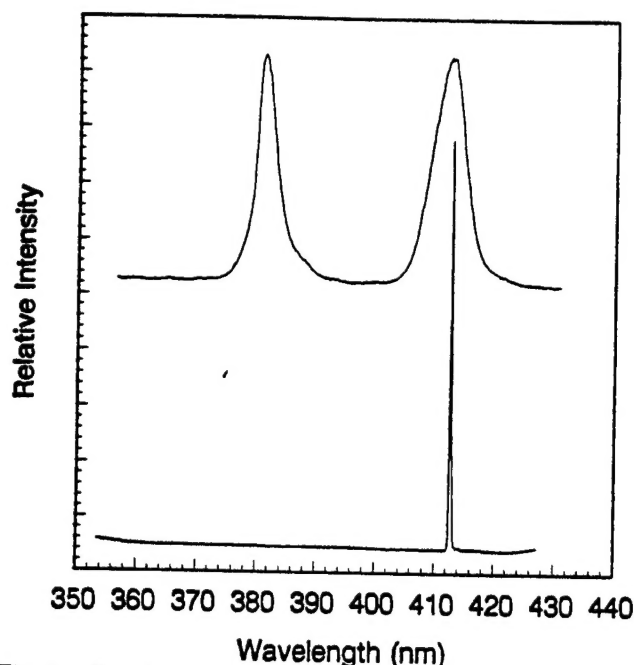


Fig. 1. Spontaneous emission and laser spectra for a Nd:ZBLAN fiber in the 360–430-nm spectral interval.

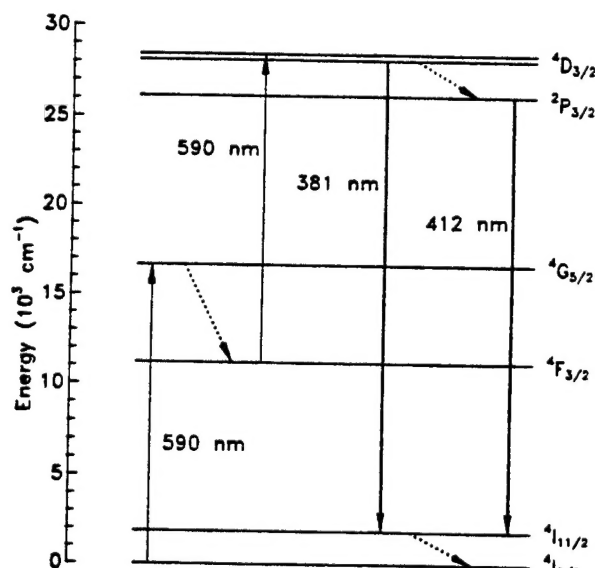


Fig. 2. Partial energy-level diagram of Nd^{3+} illustrating the absorption of two orange (~ 590 nm) photons followed by lasing on the ${}^4D_{3/2} \rightarrow {}^4I_{11/2}$ and ${}^2P_{3/2} \rightarrow {}^4I_{11/2}$ transitions of the ion in the ultraviolet and violet, respectively. The dotted lines represent nonradiative relaxation of an excited state by multiphonon emission.

~ 280 mW, the output shows signs of saturating, but, as indicated by the solid line in the figure, the overall slope efficiency exceeds 0.5%. Higher cavity output couplings have not yet been investigated, but it is expected that the optimal value will be $>0.4\%$ and that the output power and slope efficiency will both increase significantly over the values reported here. It should also be noted that the fiber exhibited several localized regions in which scattering was obvious. Continuing improvements in ZBLAN fiber fabrication will be necessary for the potential of this laser to be re-

alized. Nevertheless, the performance of the Nd violet fiber laser compares favorably with that for the recently reported room-temperature Tm:ZBLAN fiber laser¹⁰ that operates at 455 nm. Requiring two-color pumping (645 nm and 1.064 μm), the Tm:ZBLAN blue

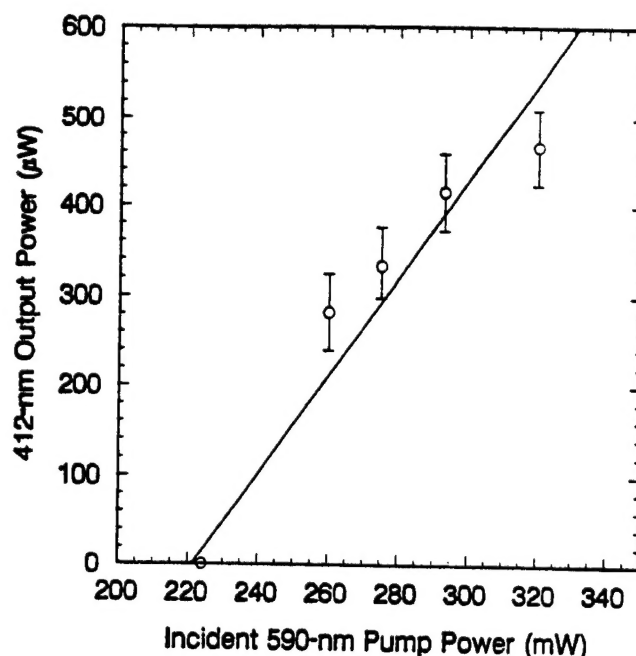


Fig. 3. Dependence of the violet laser output power on the 590-nm pump power incident on the input coupling optics. The estimated launching efficiency for the pump is 30%, and the cavity output coupling and fiber length are 0.4% and 39 cm, respectively. The solid line represents a slope efficiency of 0.5%.

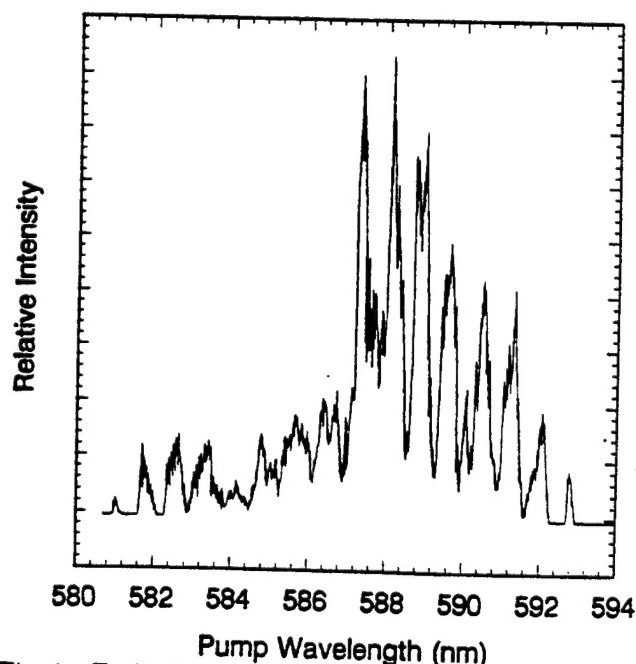


Fig. 4. Excitation spectrum for the 412-nm laser showing peak output power for pump wavelengths between ~ 587 and 589 nm. The periodic modulation of the spectrum is due to power reflected from the coupling optics.

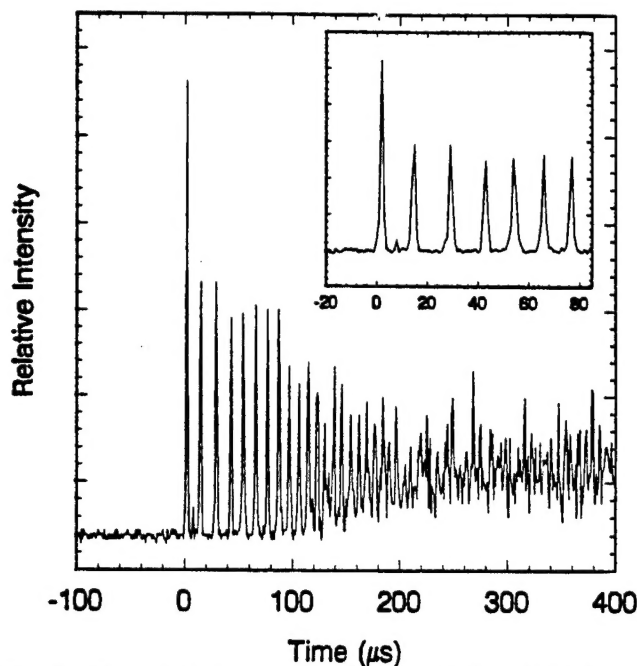


Fig. 5. Transient temporal behavior of the violet laser. The transition to cw operation occurs in $\sim 250 \mu\text{s}$. The inset is a magnified view of the first $80 \mu\text{s}$ of the waveform that was recorded for a pump power (incident on the fiber) of $\sim 450 \text{ mW}$.

laser has a slope efficiency of 1.5% and a threshold pump power (red plus infrared) of $\sim 420 \text{ mW}$.

Figure 4 displays the excitation spectrum that was obtained by recording the violet output power as the wavelength of the ring dye laser was scanned. Most of the structure in the spectrum results from interference effects between the input (flat) mirror and the fiber end that modulates the pump power coupled into the fiber by several percent.⁷ Lasing is observed for pump wavelengths lying between 581 and 593 nm, but the device operates most efficiently when pumped in the 587–589-nm region. As observed previously for other rare-earth-doped ZBLAN fiber lasers, the Nd:ZBLAN laser is relatively insensitive to pump wavelength because the disordered nature of the glass host results in broadened gain and absorption spectral profiles.

A waveform representative of those observed when the pump beam (power incident on the fiber of $\sim 450 \text{ mW}$) is chopped is shown in Fig. 5. Lasing begins $\sim 0.5 \text{ ms}$ after the pump is applied and, initially, exhibits relaxation oscillations having a periodicity of $\sim 15 \mu\text{s}$ (the inset of Fig. 5 gives an expanded view

of the early portion of the waveform). The amplitude of the pulses decreases rapidly, and, after $\sim 250 \mu\text{s}$, the output is continuous.

In summary, cw lasing in the violet (412 nm) has been observed from a Nd:ZBLAN fiber at room temperature. Roughly 0.5 mW of power has been obtained with an output coupling of 0.4%, and $\sim 320 \text{ mW}$ of pump power at $\sim 590 \text{ nm}$. The excitation spectrum extends from 581 to 593 nm, and, although pumping this laser in the orange is not practical at present, preliminary experiments in which the fiber is excited at two wavelengths—680 and 805 nm—indicate that diode laser pumping of this oscillator should be feasible.

This research was supported by the U.S. Air Force Office of Scientific Research and the Advanced Research Projects Agency.

References

1. Strictly speaking, the visible fiber lasers utilizing ZBLAN glass as a host are generally not pumped by upconversion because the rare-earth concentrations are typically only 1000 ppm and the term upconversion has traditionally been reserved for interactions between two excited ions. However, the term has recently come to be associated with any process—such as the sequential absorption of two or more photons—by which low-energy (i.e., red or infrared) photons are converted to visible photons in a rare-earth-doped solid.
2. J. Y. Allain, M. Monerie, and H. Poignant, *Electron. Lett.* **26**, 166 (1990).
3. J. Y. Allain, M. Monerie, and H. Poignant, *Electron. Lett.* **26**, 261 (1990).
4. T. J. Whitley, C. A. Millar, R. Wyatt, M. C. Brierley, and D. Szebesta, *Electron. Lett.* **27**, 1785 (1991).
5. R. G. Smart, D. C. Hanna, A. C. Tropper, S. T. Davey, S. F. Carter, and D. Szebesta, *Electron. Lett.* **27**, 1307 (1991).
6. S. G. Grubb, K. W. Bennett, R. S. Cannon, and W. F. Humer, *Electron. Lett.* **28**, 1243 (1992).
7. D. S. Funk, J. W. Carlson, and J. G. Eden, *Electron. Lett.* **30**, 1859 (1994).
8. F. Tong, R. M. Macfarlane, and W. Lenth, in *Conference on Quantum Electronics and Laser Science*, Vol. 12 of 1989 OSA Technical Digest Series (Optical Society of America, Washington, D.C., 1989), paper THKK4.
9. M. F. Joubert, B. Jacquier, C. Linarès, and R. M. Macfarlane, *J. Lumin.* **47**, 269 (1991).
10. M. P. LeFlohic, J. Y. Allain, G. M. Stéphan, and G. Mazé, *Opt. Lett.* **19**, 1982 (1994).